CHALMERS
UNIVERSITY OF TECHNOLOGY

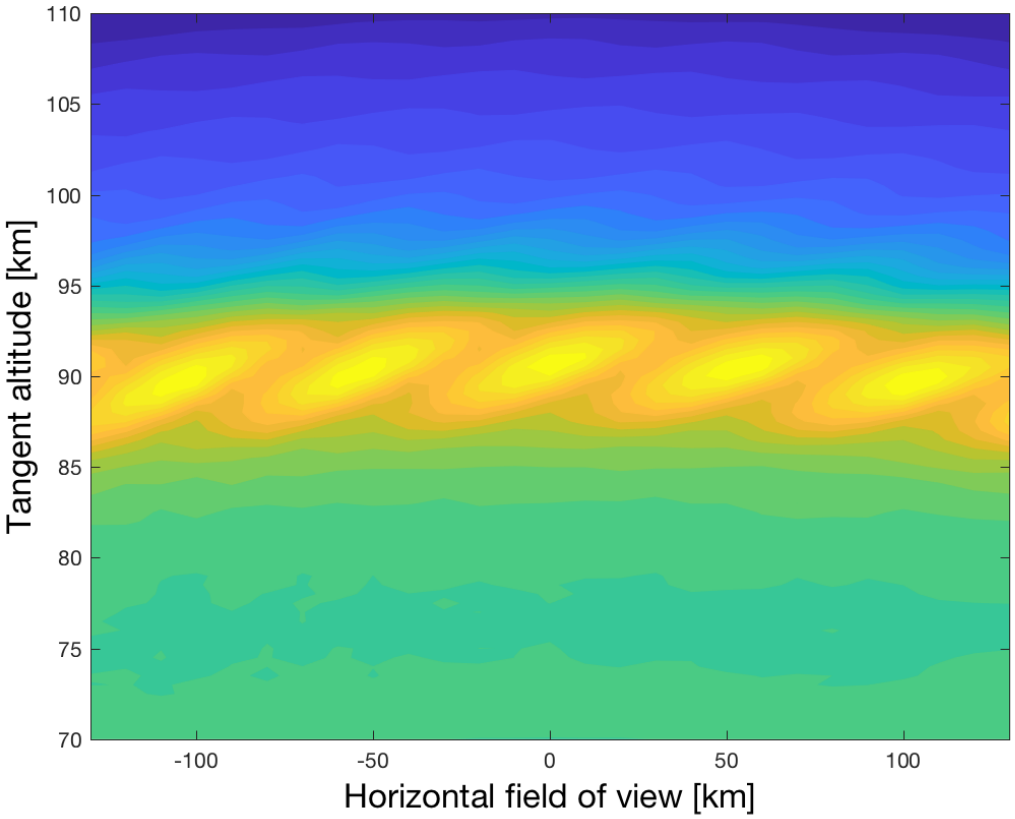

A 3D-model for O_2 airglow perturbations induced by gravity waves in the upper mesosphere

A forward model for the new Swedish satellite MATS

Master's thesis

ANQI LI

Department of Earth and Space Sciences
CHALMERS UNIVERSITY OF TECHNOLOGY
Gothenburg, Sweden 2017

Master's thesis 2017

A 3D-model for O_2 airglow perturbations induced by gravity waves in the upper mesosphere

A forward model for the new Swedish satellite MATS

ANQI LI

CHALMERS
UNIVERSITY OF TECHNOLOGY

Department of Earth and Space Sciences
Chalmers University of Technology
Gothenburg, Sweden 2017

A 3D-model for O_2 airglow perturbations induced by gravity waves in the upper mesosphere
A forward model for the new Swedish satellite MATS
ANQI LI

Supervisor: Ole Martin Christensen, Department of Meteorology, Stockholm University
Examiner: Donal Murtagh, Department of Earth and Space Sciences, Chalmers

Master's Thesis 2017
Department of Earth and Space Sciences
Chalmers University of Technology
SE-412 96 Gothenburg
Telephone +46 31 772 1000

Cover: A simulated satellite image from the model.

A 3D-model for O_2 airglow perturbations induced by gravity waves in the upper mesosphere
A forward model for the new Swedish satellite MATS
ANQI LI
Department of Earth and Space Sciences
Chalmers University of Technology

Abstract

To investigate the influence of atmospheric waves in the mesosphere, a new Swedish satellite MATS (Mesospheric Airglow/Aerosol Tomography and Spectroscopy) will be launched in 2019. It will observe infrared emissions at 762 nm from the $O_2(b^1\Sigma_g^+)$ airglow in the region of 70 - 110 km altitude. As a part of the design work for the MATS project, an accurate forward model is needed to estimate what MATS is expected to measure. The results from this model will be used to evaluate the retrieval methods for processing the measurements from MATS.

In this thesis project, a gravity wave model and a photochemistry model were coupled to simulate both the day- and nightglow emission fields in three spatial dimensions and time. Simulated satellite images were generated taking into consideration the sphericity of the Earth and the limb-viewing geometry of MATS. Simulation parameters were set according to the preliminary design of the instrument, such as the satellite orbit, image resolution and spectral selections. These satellite images were the first simulated airglow limb images made for the MATS project.

By analysing the output data, the relations between wave parameters and airglow perturbations were investigated. It was shown that wave patterns can be easily observed between 85 - 105 km due to the relatively large perturbation in airglow emissions. The O_2 airglow emission field was found to be highly sensitive to atomic oxygen concentration field as an input. Furthermore, as expected, wave patterns projected on simulated satellite images largely depend on the horizontal orientation of the wave propagation. This implies that a tomographic reconstruction is needed when the angle between the wave front and the limb-viewing direction is large. Finally, limitations of the model were discussed.

Keywords: MATS, internal gravity wave, mesosphere, O_2 airglow,

Acknowledgements

I would like to express my appreciation to Donal and Ole Martin, who brought me to the wonderland of gravity waves and airglow chemistry. Under their great supervisions, my interests and knowledge in atmospheric dynamics and chemistry has become much deeper. Thanks to the master thesis project, I feel grateful to be involved in the MATS project and to earn great experience in working at the department of Earth and Space Sciences at Chalmers.

In addition, I would like to say thank you to my high school teachers in physics and mathematics, who gave me the spirit of solving problems and discover principles of the nature.

Last but not least, I would like to thank my family and friends for supporting me in studying in Sweden and giving me much of their love and kindness. Without any of these components, none of the work for the master thesis project could have possibly been done.

Thanks! Xiexie! Arigatou! Tack!

Anqi Li, Gothenburg, April 2017

Contents

List of Figures

List of Tables

1

Introduction and background theories

The weather in the mesosphere has been affected by human activity since the start of the industrial revolution, just like the lower atmosphere. An increase of CO_2 concentration gives not only a warming effect in the lower atmosphere, but also a cooling effect in the middle atmosphere. It is predicted that a significant reduction in the mean temperature by 10 K will occur with a doubling of CO_2 concentrations (Roble and Dickinson (1989)). A large stratospheric ozone hole was discovered by Farman et al. (1985) over the Antarctica. Scientists have suggested that the ozone loss was caused by anthropogenic released chlorofluorocarbons (CFCs). However, the full implications of climate change are far from understood. For instance, atmospheric models used in this region have limited ability to predict future changes. One of the limiting factors is large uncertainty in the characteristics and the global distribution of gravity waves. Recent research has revealed that waves can link together different parts of our climate system over long distances (Brasseur and Solomon (2005)). Species with short chemical lifetime in the middle atmosphere such as stratospheric ozone are strongly influenced by photochemical fluctuations induced by gravity waves. Thus, by understanding, measuring and quantifying atmospheric waves in the mesospheric region, seasonal forecasts from climate models can be improved. Similar to the temperature distribution in the Earth's atmosphere, the level of understanding of ozone layer and other problems that involve gravity wave transports and mixing can be also improved.

Although the role of gravity waves on the Earth's atmosphere has been studied over the past 5 decades, many scientific questions are still remained. To improve our understanding of gravity waves in the mesosphere, the MATS satellite will be launched in 2019. This satellite will provide the first 3 dimensional structures of gravity waves in the upper mesosphere, by making use of optical phenomena that are specific for the mesosphere. These are the light emitted from excited oxygen molecules called oxygen airglow, and the light scattered by aerosol particles in the form of "noctilucent clouds" (NLCs). As a part of the preparatory work, an accurate forward model of what MATS is expected to observe is required.

The objective of this thesis project is to implement a three dimensional model of gravity waves, and couple it with a photochemistry model to investigate how these waves modify the airglow emissions from excited oxygen molecules in the mesosphere. According to the preliminary design of the MATS project, simulated satellite images of the Earth's limb will be generated. The results can be used for the evaluation of the retrieval methods for processing the measurements from MATS.

1.1 Atmospheric structure and dynamics

The Earth's atmosphere is divided into different layers based on different characteristics. One of the most common divisions of the atmosphere is based on its vertical temperature gradient which is either positive or negative, as shown in Figure 1.1. The mesosphere is one of the "spheres" among others, where the temperature gradient is negative and it ranges approximately from 50 km altitude to 100 km. The top of mesosphere, the mesopause, is often not clearly defined but can be considered as a region between 80 and 100 km, where the coldest temperatures in the atmosphere can be found. Above the mesopause is the thermosphere, in which the vertical temperature gradient is positive. Below the mesosphere are stratosphere and troposphere. Troposphere, stratosphere and mesosphere are collectively referred as the homosphere, where the composition of the atmosphere can be roughly regarded as constant, with the major constituents N_2 and O_2 made up around 80% and 20%, respectively, of the total number density.

Figure 1.2 shows the zonal mean temperature distribution and illustrates the general circulation of the middle atmosphere. Although the summer pole receives much more solar radiation than the winter pole, the coldest region on the earth is found in the summer mesopause. Also, the tropical tropopause is cooler than its counterpart at the same altitude. The cold temperature is due to the large scale meridional pole to pole circulation in the mesosphere, as well as the upward motion above the summer pole and the tropical region. It is based on simple thermodynamic considerations – an air parcel displaced upward (pressure decreased) will expand and cool down. The meridional wind (wind speed in the latitudinal direction) can be observed and verify the theory of general circulation in the middle atmosphere (Nastrom et al. (1982)). It is now recognized that an essential component of the general circulation is the deposition of energy and momentum driven by atmospheric waves. More precisely, the circulation in the stratosphere, also called Brewer-Dobson circulation, is driven by planetary waves which have larger wavelengths. The circulation in the mesosphere is driven by gravity waves which have smaller wavelengths. Thus understanding the behaviour of gravity waves plays a crucial role to the improvement of atmospheric models in the mesosphere.

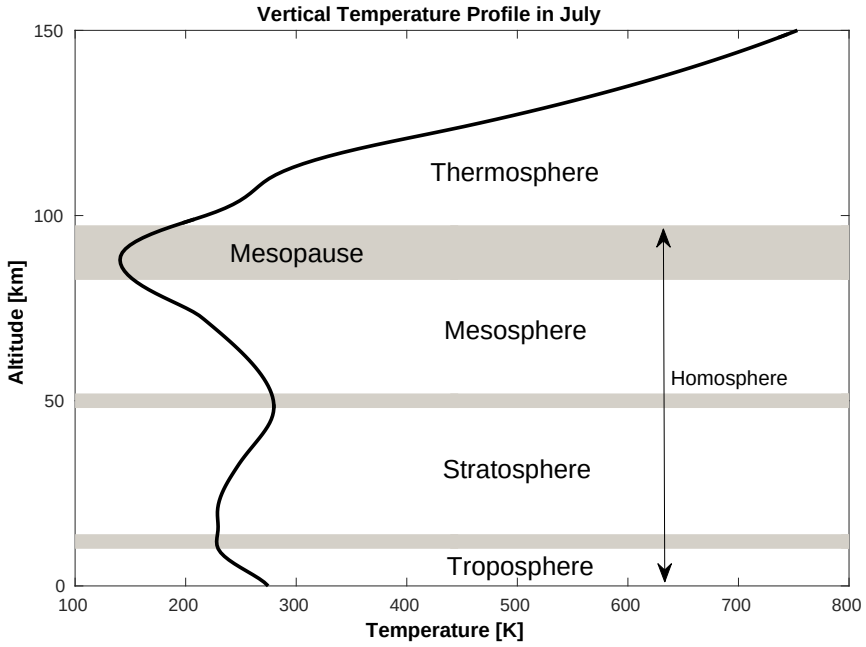

Figure 1.1: Divisions of the atmosphere based on vertical temperature gradient or composition. Vertical temperature profile is obtained from MSIS-90 model in July at latitude of 80°S.

1.2 Internal gravity waves

Environmental lapse rate is defined as the rate of decreasing temperature with increasing altitude

$$\Gamma_E = -\frac{dT}{dz}. \tag{1.1}$$

Combining the hydrostatic equation and the expression for potential temperature, a dry adiabatic lapse rate (ALR) Γ_d can be derived as 10 K/km. In a stable atmospheric condition, where Γ_E is less than ALR, a parcel of air that is uplifted will cool to lower temperature than its new surroundings along the ALR. Hence the air parcel will be denser than its surroundings and will tend to fall back to its original altitude (pressure level). When the parcel of air is pushed down, it will tend to rebound for the same reason. In other words, air that is forced to displace will tend to return to its original altitude by buoyancy force and gravity force, resulting in an up-and-down bouncing motion. As shown in Figure 1.3, it is identical with a physical model of a weight that is connected to a spring. Such displacements of air can be generated by mountains, hills, thunderstorms, velocity jets, large explosions, etc.

As can be examined from vertical temperature gradients shown in Figure 1.1, the stratosphere and mesosphere are more likely to exhibit static stability conditions than in the troposphere. One of the examples of gravity waves is lee wave, or known

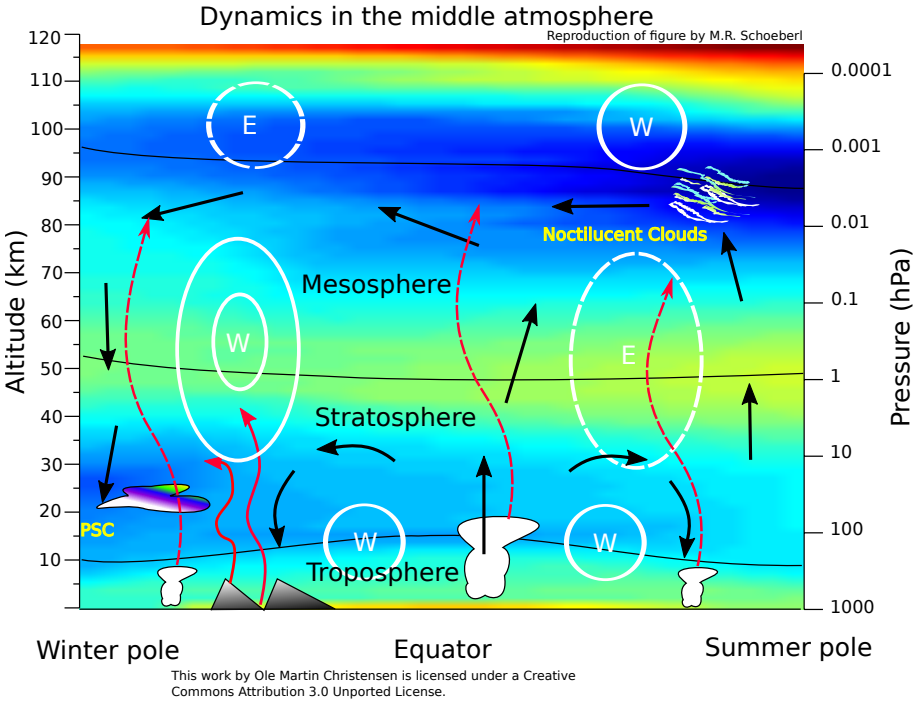

Figure 1.2: An illustration of the dynamics in the middle atmosphere. Black arrows indicate general circulations both in the stratosphere and in the mesosphere. The background colour indicates the zonal mean temperature obtain from CIRA-86 model, with red and blue indicating hot and cold temperature, respectively. Dashed and solid red lines show internal gravity waves and planetary waves, respectively. Dashed and solid white circles illustrate the easterlies and westerlies zonal wind, respectively.

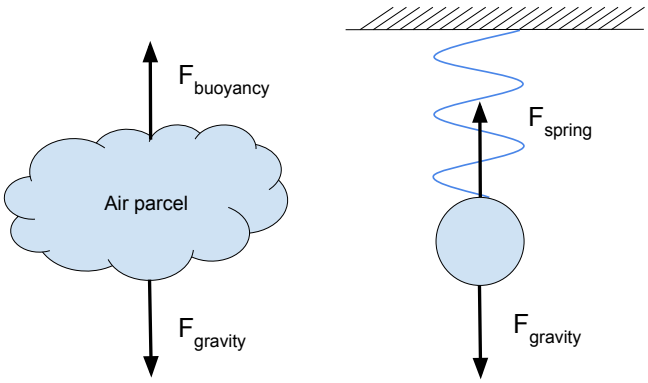

Figure 1.3: A physical model of an air parcel under a stable atmospheric condition is identical with a weight that is connected to a spring.

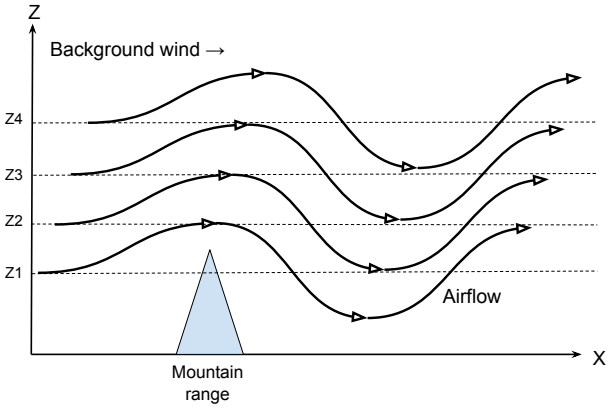

Figure 1.4: An illustration of air flow over the mountain range under a stable atmospheric condition, as one of the examples of gravity wave.

as mountain wave. As air is blown against a large topographic feature, it is forced to rise. If the atmosphere is in a stable condition, then on the lee side of the mountain it will tend to rebound to the original altitude. However, its momentum is such that it will shoot past its original altitude and go lower than it was before. It then will rise again to come back to its original height. It will again overshoot, this time going too high, and so on. This up-and-down motion pushes layers above and below the air parcel, and thus gravity wave is propagated to even higher (or lower) altitudes (see Figure 1.4).

Gravity waves have impacts on atmospheric density profiles, temperature profiles as well as wind profiles in both vertical and horizontal directions. Especially in the higher altitude region where air densities are low, the amplitudes of the wave fluctuations will become large. As a result, gravity waves may cause perturbations in the mesosphere so large that a considerable influence on the mean atmospheric state can not be neglected. As mentioned above, gravity waves play a crucial role to the general circle in the mesosphere transporting energy and trace chemical species. Since perturbed air density and temperature alter the physical phases of water in the air, as well as local photochemical reactions via variations in associated rate coefficients and gas distributions. Characteristics of the waves can be captured by sensing these optical phenomena on clouds and airglow as shown in Figure 1.5.

1.3 Airglow

Airglow is the optical emissions from excited chemical species in the atmosphere. Airglow causes the night sky never to be completely dark when observing from the ground. A thin greenish layer on the night side of the Earth's atmosphere can also be seen from the space (Figure 1.6). It is easier to detect airglow emissions at night because of the weak intensity and spectral region of the emissions. In the day the scattered sunlight is abundantly dominant even though airglow intensities are

Figure 1.5: Stripped airglow observed from the ground over Maine, USA (left). Image is taken by Mike Taylor and Sonia MacNeil. A satellite image (MODIS imager on board the Terra satellite) of a wave cloud forming off of Amsterdam Island in the far southern Indian Ocean (right). Image from NASA.

Figure 1.6: The airglow above the horizon captured from the International Space Station. Image from NASA.

orders of magnitude larger than those in the night. Nevertheless, depending on the time of the day at which observations are made, airglow is called either dayglow or nightglow. Common airglow emissions are from excited atoms and molecules driven by photons from the sun, such as excited OH , NO, Na, Li and O_2. This thesis addresses airglow emissions from $O_2(b^1\Sigma_g^+)$ at a wavelength around 762 nm in the region of $70 - 110$ km altitude.

Emission from an excited species X* is described by the rate law

$$V = A \cdot [X^*], \tag{1.2}$$

where $[X^*]$ is the concentration of the excited species X*. In this case, [X*] will be replaced by the number density of $O_2(b^1\Sigma_g^+)$ in units of *molecules* per cm^3. A is the Einstein A coefficient for spontaneous emission from the excited species. V is called the volume emission rate in units of *photons* per cm^3 per *second*. Because the present thesis only addresses one species, A can be treated as constant. Therefore, the volume emission rate purely depends on the concentration of the species.

The concentration [X*] can be calculated according to photo-chemical equilibrium hypothesis, which is a balance between production rates and loss rates. Detailed calculations and the proposed mechanisms will be further discussed in the following section. Production and loss rates depend on the concentrations of reactants and rate coefficients for different reactions. Some of the reactions associate with temperature dependent rate coefficients. To summarise, the intensity of a certain airglow depends on concentrations of reactants that are producing or quenching the excited species and local temperatures.

Altitude profiles of airglow emissions provide valuable information on the vertical distributions of the specific species. In the early years, these profiles have been obtained by measuring variation in intensity with viewing angles from the ground or by rocket measurements estimating the integrated overhead intensity. Although methods mentioned above are cheaper and easier to maintain, they can not provide results with high spatial coverage. In recent years, satellite measurements provide prominent results of global distribution of airglow emissions in high spatial coverage. Optical Spectrograph and Infrared Imaging System (OSIRIS) on board Odin satellite has observed the O_2 A-band airglow emissions in the mesosphere and lower thermosphere (MLT) (Murtagh et al. (2002)). Other instruments such as the Wind Imaging Interferometer (WINDII) on NASA's Upper Atmosphere Research Satellite (UARS) (Shepherd et al. (2012)) have also measured the O_2 A-band emissions.

1.4 The MATS mission

MATS is a satellite mission of Sweden, funded by the Swedish National Space Board (SNSB). The small, low-cost research satellite will be launched in 2019 into a 600 km sun-synchronous orbit. Two science instruments, namely the limb imager and the nadir imager are on board.

MATS is designed to study the horizontal and vertical atmospheric structure in the mesosphere and lower thermosphere by limb imaging in combination with tomographic retrieval techniques. As the gravity waves can alter the appearance of noctilucent clouds (NLCs) and oxygen airglow, fluctuations in UV scattering light (ca. 260-310 nm) and infrared emissions (ca. 758-768 nm) from excited O_2 are detectable. Observations will be done by mainly imaging the limb of the atmosphere at six different wavelengths/channels (see Tabel 1.1). The vertical field of view for IR imager and UV imager are set to be 75-110 km and 70-90 km at tangent point, respectively. The horizontal limb field of view is set to be $\pm$125 km for all channels. The viewing direction is along the track of satellite orbit. More precisely, as MATS will observe gravity waves whose horizontal wavelengths are smaller than 100 km, imaging resolution must be good enough. This requires the vertical resolution of UV and IR channels to be 0.2 km and 0.4 km, respectively. Horizontal resolutions for UV and IR channels should be 5 km and 10 km, respectively.

In order to evaluated the instrument design, an accurate forward model to generate

Table 1.1: Spectral selection of the limb imaging

Channel	Central wavelength	Band width
UV 1	270 nm	3 nm
UV 2	304.5 nm	3 nm
IR 1	763 nm	8 nm
IR 2	762 nm	3.5 nm
IR 3	754 nm	3 nm
IR 4	772 nm	3 nm

atmospheric signal is needed. This master thesis project will contribute to the estimation of what MATS is expected to observe as well as the development of retrieval methods from the measurement data.

2

Gravity wave model description

In this Chapter, the implementation of a simple gravity wave model based on linearized equations will be described. Following the model developed and described by Hines (1960) and Frederick (1979), spatial dimensions are expanded to 3D by introducing a parameter for the angle of wave propagation direction. Modifications are made to the wave amplitude and dissipation as well.

2.1 From a 2D-model to a 3D-model

Linear theory has been used for deriving the mathematical models for internal gravity waves. As stated in earlier studies, the linearized equations do have advantages in computational speed, understandable, but also have limitations in inaccuracy and other practical limitations. A linear wave model and a nonlinear wave model were compared by Dörnbrack and Nappo (1997). They concluded that essentially similar results are obtained from each model for the important wave parameters and dynamic effects. In this thesis, the effects of the Earth's rotation and air viscosity are neglected. The perturbations of temperature and air density are assumed smaller than the background values, and are caused only by gravity waves. Under the principle assumptions that the atmosphere is isothermal and there are no background winds, equations which govern the oscillations are presented in Eq 2.1 - 2.6.

Temperature perturbation is

$$T' = \bar{T} A \, e^{z/2H} (\gamma - 1) \{ \omega^2 k_z \cos\theta - g[\gamma\omega^2/C^2 - k_h^2] \sin\theta \}, \tag{2.1}$$

bulk density perturbation is

$$n'_M = \bar{n_M} A \, e^{z/2H} \{ \omega^2 k_z \cos\theta + [(1 - \gamma/2) k_h^2 g + (\omega^2 - k_h^2 C^2)/2H] \sin\theta \}, \tag{2.2}$$

horizontal velocity is

$$v_h = A \, e^{z/2H} \omega k_h C^2 \{ k_z \cos\theta + [(1 - \gamma/2) g/C^2] \sin\theta \}, \tag{2.3}$$

and vertical velocity is

$$v_z = A \, e^{z/2H} \omega (\omega^2 - k_h^2 C^2) \cos\theta, \tag{2.4}$$

where the phase angle is

$$\theta = \omega t - k_h h - k_z z, \tag{2.5}$$

and dispersion relation is

$$\omega^4 - \omega^2 C^2 (k_h^2 + k_z^2) + (\gamma - 1) g^2 k_h^2 - \gamma^2 g^2 \omega^2 / 4C^2 = 0, \tag{2.6}$$

where ω = wave frequency = 2π/wave period,
k_h = horizontal wavenumber = 2π/horizontal wavelength,
k_z = vertical wavenumber = 2π/vertical wavelength,
t, h, z = time, horizontal distance, altitude,
g = gravitational acceleration,
C = speed of sound,
$\gamma = c_p/c_y$ ratio of specific heats,
$\bar{n_M}, \bar{T}$ = background density, background temperature,
H = scale height,
A = reduced amplitude.

The number density perturbation in Eq 2.2 can be only applied to the bulk atmosphere n_{O_2} and n_{N_2} – the major compositions of n_M. Number density perturbation for minor constituents such as atomic oxygen n'_O is obtained as follows

$$n'_O = \bar{n_O} A \, e^{z/2H} \{\omega^2 k_z \cos\theta + [(1 - \gamma/2) k_h^2 g - (\omega^2 - k_h^2 C^2)(\frac{1}{\bar{n_O}} \frac{\partial \bar{n_O}}{\partial z} + \frac{1}{2H})] \sin\theta\}. \tag{2.7}$$

The Dispersion relation in Eq 2.6 relates the wave frequency to the wave structure and the physical characteristics of the atmosphere. It fixes one of the wave parameters based on the other two parameters. For example, once values of k_h and ω are given, the value of k_z is fixed. The quantity of 'reduced amplitude' A in unit of $[km\ s^2]$ represents the physical energy input from the initial perturbation, e.g. the size of the mountains, the strength of thunderstorms or the power of explosions. Parameters such as k_h, k_z, ω and A typically occur at the mesospheric region must be determined from either observations or more sophisticated dynamical model. In this thesis project, a temperature amplitude at 90 km around ± 10 K with a vertical wavelength of $2 - 8$ km and wave period between $1 - 2.5$ h are in focus, which implies horizontal wavelength of $21 - 208$ km and a reduced amplitude between $0.3 - 28.6$ $km\ s^2$. The choice of wave period relates to photochemical lifetimes of odd oxygen family, which is shown in Figure 3.2 and will be discuss in Section 3.2. The choice of horizontal and vertical wavelengths should not be smaller than 5 times the resolution of simulation domain. Figure 2.1 shows the relations between three wave parameters l_h, l_z and wave period in minute, as well as relations with temperature perturbations at an altitude of 90 km when A is fixed to 1 $km\ s^2$. g, C, γ, H are treated as constants throughout the altitude range in the present model and their values are presented in Table B.2.

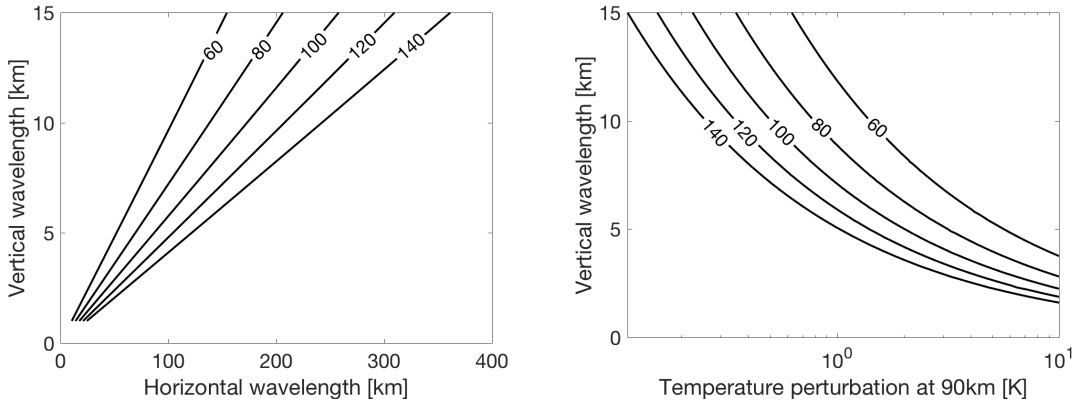

Figure 2.1: The relation between wave period in $[minutes]$ with horizontal wavelength in $[km]$ and vertical wavelength in $[km]$ (left). The relation between wave period in $[minutes]$ with vertical wavelength in $[km]$ and temperature perturbation at 90 km altitude in $[K]$ when $A = 1$ $[km\ s^2]$ (right). Wave period ranges from 60 to 140 minutes with 20 minutes interval.

The model presented by Frederick (1979) was a 2-dimensional model, including the vertical component and the horizontal component in space. To expand the model into 3 dimensions as one of the objectives of this thesis, the horizontal component is further divided into 2 components, x and y. Here, the horizontal wavenumber in x direction and y direction, k_x and k_y, respectively, must be introduced. Consequently, the phase angle θ and the horizontal wavenumber k_h in Eq 2.1 - 2.7 are replaced by the following relations

$$\theta = \omega t - k_x x - k_y y - k_z z, \tag{2.8}$$

$$k_h^2 = k_x^2 + k_y^2,\ k_x = k_h \cos\xi,\ k_y = k_h \sin\xi, \tag{2.9}$$

where the angle ξ defines the orientation of the wave front at the horizontal x-y plane. If ξ has a value of $\pi/2$, the wave fronts become parallel to the y-axis. The relation is illustrated in Figure 2.2. Horizontal velocity v_h in Eq 2.3 needs to be divided into v_x and v_y as well

$$v_h^2 = v_x^2 + v_y^2,\ v_x = v_h \cos\xi,\ v_y = v_h \sin\xi. \tag{2.10}$$

2.2 Wave amplitude

To ensure the wave amplitude will not be affected by the chosen value of scale height H, which is assumed to be constant in the model, the term $Ae^{z/2H}$ in Eq 2.1, Eq 2.2, Eq 2.3, Eq 2.4 and Eq 2.7 is replaced by

$$Amplitude(z) = A\ e^{z/2H} = c/\sqrt{\bar{n_M}(z)}. \tag{2.11}$$

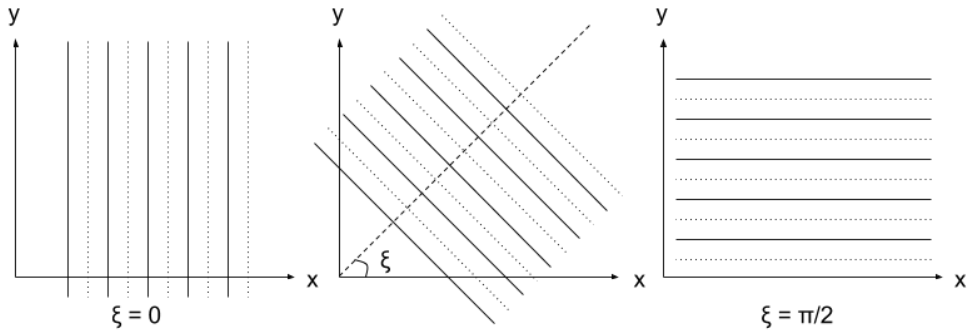

Figure 2.2: An illustration of the relation between the angle ξ and the orientation of the wave front at the horizontal x-y plane. Solid lines represent the wave crest and dashed lines represent the wave trough.

When $z = 0$, the newly introduced constant c can be determined.

$$c = A\sqrt{\bar{n_M}(z=0)}. \tag{2.12}$$

This can be understood by assuming the kinetic energy density must remain constant without dissipation

$$\frac{1}{2}n_M|v|^2 == const. \tag{2.13}$$

where n_M and v represent the density and wind speed of the air, respectively. Replacing $n_M = n_{M_0}\ \exp(-z/H)$ to the above equation, it can be rewritten to

$$\begin{aligned} |v(z)| &= const.\ n_M^{-1/2} \\ &= const.\ n_{M_0}^{-1/2}\ \exp(-z/H)^{-1/2} \\ &= A\ \exp(z/2H), \end{aligned} \tag{2.14}$$

where n_{M_0} represents the density of the air at sea level. In other words, wave amplitude grows exponentially with altitude and the reduced amplitude can be expressed as

$$A = const.\ n_{M_0}^{-1/2}. \tag{2.15}$$

Eq 2.15 is identical to Eq 2.12. By doing so, the wave amplitude is increasing exponentially with decreasing air density. Figure 2.3 shows the vertical structure of the background temperature and number density of atomic oxygen (blue dotted lines). The perturbed temperature and number density of atomic oxygen without consideration of dissipation are shown as magenta dashed lines. All lines are taken at the same instant of time $t = 0$ and the same horizontal location $x = y = 0$. Temperature perturbations are $\pm 2.5\ K$ at 80 km and $\pm 5\ K$ at 90 km. The wave amplitude grows rapidly with increasing altitude so that the temperature perturbation at 100 km is as large as $\pm 15\ K$. On the other hand, the oscillations on atomic oxygen concentration do not grow rapidly with altitude. This is because a peak in

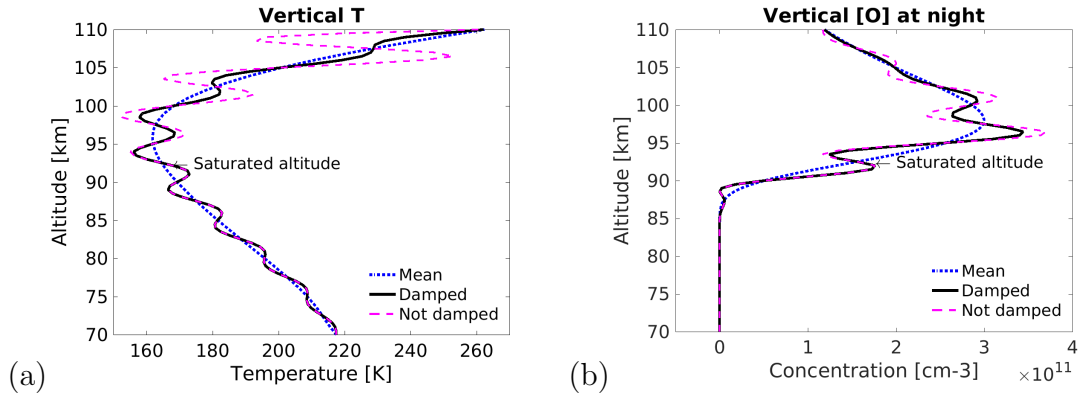

Figure 2.3: The temperature and the atomic oxygen number density under the influence of internal gravity wave with wave period of $2\pi/\omega = 1\ hour$, vertical wavelength of $2\pi/k_z = 5\ km$, horizontal wavelength of $2\pi/k_h \approx 52\ km$ and reduced amplitude of $A = 1\ km\ s^2$. The background state of temperature and bulk number density are taken from the MSIS-90 model at a latitude of 0 in June. The background state of atomic oxygen profile is parametrized according to Eq 3.2 and Table B.2. (a):The vertical profile of temperature at $x = y = 0$ and $t = 0$ for the background state (blue dotted line), perturbed by a gravity wave with dissipation above saturated altitude (black solid line) and without dissipation (magenta dashed line). (b):Same to (a) but the number density of atomic oxygen.

the background state of $[\bar{O}]$ occurs at 98 km and since the vertical gradient is large below the peak, the perturbation becomes large as implied in Eq 2.7. $n'_O/\bar{n_O}$ are $\pm 80\%$, $\pm 35\%$ and $\pm 20\%$ at 90, 95 and 100 km, respectively.

However, the wave amplitude will have grown large enough that at a certain altitude, a super-adiabatic lapse rate will occur in the perturbed temperature, i.e. the temperature decreases with altitude at a rate of greater than 10 K/km. For instant, in Figure 2.3(a) the perturbed temperature gradient $-dT/dz$ of the magenta dashed line is greater than 10 K/km around altitude of 95 , 100 , 105 , 110 km. At this point, the atmosphere is no longer statically stable enough for the propagation of internal gravity wave, i.e. a displaced air parcel does not have the tendency to return to its original position (see Section 1.2). Waves become unstable and are said to break at the altitude where a super-adiabatic lapse rate is first reached. Because of the complexity of the non-linear wave theory and the uncertainty of the real atmosphere, the breaking of the wave is difficult to model. One of the solutions is to introduce a constant damping factor δ (Liu and Swenson (2003)), so that

$$Amplitude(z) = A\ e^{(1-\delta)z/2H}. \tag{2.16}$$

When $\delta = 0$, no dissipation is present and the wave amplitude grows exponentially with increasing altitude; when $\delta = 1$, it simulates 'saturated waves', whose amplitude does not grow and stays constant with altitude; when $\delta > 1$, it represents large dissipation and wave amplitude decreases with increasing altitude. Even though the dissipation rate should not be a constant in the real atmosphere, the damping factor δ was set to be constant throughout the altitude range by Liu and Swenson

(2003). An alternative solution is to let the wave amplitude remain constant once it reaches a certain limit, while allowing it to grow exponentially below the limit. This is equivalent to applying conditions to Eq 2.16 as following

$$Amplitude(z) = A\ \exp[z/2H + \delta(z_s - z)/2H],\ \text{where}\ \delta = \begin{cases} 0, & \text{if } z < z_s \\ 1, & \text{if } z \geq z_s \end{cases}, \quad (2.17)$$

where z_s is defined as the saturated altitude where the super-adiabatic lapse rate first occurs. To find out the saturated altitude z_s needs to compute where the environmental lapse rate (Γ_e) of the perturbed temperature profile is first equal or greater than dry adiabatic lapse rate $\Gamma_d = 10\ K/km$,

$$\begin{aligned} \Gamma_e(x, y, z, t) &= -\frac{dT(x, y, z, t)}{dz}, \\ z_s(x, y, t) &= min\{z|\Gamma_e(x, y, z, t) \geq \Gamma_d\}, \end{aligned} \quad (2.18)$$

where dT/dz is calculated numerically from a perturbed temperature profile without dissipation. Corresponding to the modification shown in Eq 2.11, wave amplitude is modeled as

$$Amplitude = \begin{cases} c/\sqrt{\bar{n_M}(z)}, & \text{if } z < z_s \\ c/\sqrt{\bar{n_M}(z_s)}, & \text{if } z \geq z_s \end{cases}. \quad (2.19)$$

Black solid lines in Figure 2.3 show the perturbed temperature and atomic oxygen concentration with the consideration of wave damping above the saturated altitude. Since dissipation is introduced above the saturated altitude, the kinetic energy density E_k is no longer a constant in this region. By calculating E_k as

$$E_k = \frac{1}{2} n_M v^2,\ \text{where}\ v^2 = v_x^2 + v_y^2 + v_z^2, \quad (2.20)$$

Figure 2.4(a) verifies that the kinetic energy density decreases exponentially above the saturated altitude and Figure 2.4(b) and (c) show the wave amplitude keeps constant above the saturated altitude. Wave parameters in Figure 2.4 are the same as those in Figure 2.3.

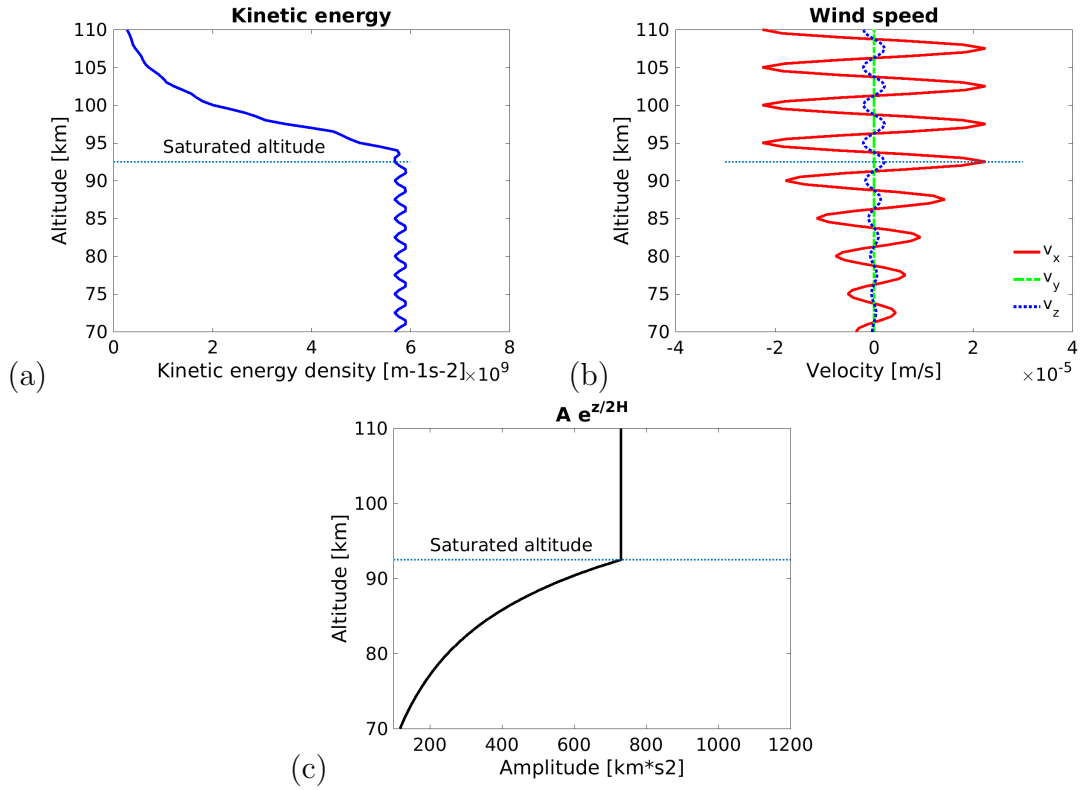

Figure 2.4: (a): The vertical profile of kinetic energy density at an instant time $t = 0$ at $x = 0$ and $y = 0$ (black solid line). The mean kinetic energy density (blue dashed line) is calculated by averaging over time and horizontal distances throughout the domain. Wave parameters are the same as those in Figure 2.3. (b): Vertical profiles of velocities v_x, v_y and v_z when $\xi = 0$. (c): Vertical profile of wave amplitude computed as in Eq 2.19 at $x = 0$, $y = 0$ and $t = 0$.

3

Airglow photochemistry model description

In this Chapter, parametrisation of atomic oxygen concentration will be first discussed. Together with molecular oxygen and nitrogen concentrations, they will be used as inputs to derive ozone and excited molecular oxygen, specifically $O_2(b^1\Sigma_g^+)$, concentrations. The equations are based on the photochemical reaction processes proposed by recent studies. Associated photolysis rates and solar excitation rates will also be calculated according to a simplified radiative transfer model.

3.1 The background state

The background state is assumed to be steady and horizontally uniform, but still varying vertically. Vertical profiles of background temperature $\bar{T}$ and bulk density $\bar{n_M}$ are adopted from MSIS-90 (Hedin (1991)). The MSIS-90 model gives the temperature and the bulk density as functions of altitude, latitude and month. Although MATS is expected to observe in the region between $70-110\ km$, the vertical profile of bulk density is taken from $70-150\ km$ altitude, to allow calculations in the radiative transfer model discussed in Section 3.4 and 3.5. Since the region in focus is in the homosphere, the majority of atmospheric compositions are O_2 and N_2, which correspond to roughly 20% and 80% of the bulk atmosphere M. Thus the following assumption is made,

$$\begin{aligned} \bar{n_{O_2}} &= 0.2\ \bar{n_M}, \\ \bar{n_{N_2}} &= 0.8\ \bar{n_M}. \end{aligned} \tag{3.1}$$

The mixing ratio of the sum of odd oxygen is only between 2×10^{-6} and 5×10^{-2} in this region and the distributions of atomic oxygen and ozone are closely related to the incoming solar radiation. Reed and Chandra (1975) have proposed the following parametrization to approximate the atomic oxygen profile in Chapman distribution

$$\bar{n_O} = \bar{n_{Omax}} \exp[\frac{1}{2}(1 - \frac{z - z_{max}}{SH} - \exp(\frac{z_{max} - z}{SH}))], \tag{3.2}$$

where $\bar{n_{Omax}}$ represents the peak number density of atomic oxygen and z_{max} is the peak height at $\bar{n_{Omax}}$. S is a shape factor, interpreted as a parameter reflecting

Table 3.1: Values of the n_O profile key parameters used in this thesis

Symbol	Value	Unit
$\bar{n_{O}}_{max}$	3×10^{11}	$molecule/cm^3$
z_{max}	98	km
S	0.8	-
H	5.38	km

the relative importance of mixing and diffusion in the lower thermosphere, and H is the scale height of the mixed atmosphere. Very few direct measurements on atomic oxygen profiles. Melo et al. (2001) derived atomic oxygen vertical distributions from ground-base measurements of nightglow. Key parameters for Eq 3.2 were evaluated seasonally. Values adopted for the key parameters in this thesis are within the range of estimation by Melo et al. (2001). They are presented in Table 3.1, so that the resulting nightglow profile from the model is fit in the estimated values by McDade et al. (1986) from rocket measurement.

The blue dashed line in Figure 3.1(a) visualises the atomic oxygen profile according to the parametrization method described above. In comparison to the result from the model of Garcia and Solomon (1983), the current profile only approximates $\bar{n_O}$ during the night, $\bar{n_O}^{night}$. During the day the concentration of atomic oxygen does not decrease rapidly below 90 km and there appears to be a small 'tail' compared to the profile during nighttime. The reason for this will be shown in the next Section 3.2. Hence, a modification on $\bar{n_O}$ below 90 km for the day is needed. Although the transition from the midnight to the midday should be modeled smoothly with the changing solar zenith angle, the actual concentration of atomic oxygen in this atmospheric region is badly known due to lack of measurements. Thus, the following simplified modification on the $\bar{n_O}^{night}$ is applied to approximate $\bar{n_O}^{day}$ in order to mimic the result from the model of Garcia and Solomon (1983),

$$\bar{n_O}^{day} = \begin{cases} \bar{n_O}^{night}, & \text{when } z > 86.5\ km \\ \bar{n_O}^{night}(z = 86.5), & \text{when} z <= 86.5\ km \end{cases}. \tag{3.3}$$

3.2 Odd oxygen production and loss

The odd oxygen family is a collective term for both ozone and atomic oxygen. This concept is introduced because of the convenience for computational purposes. The ratio n_{O3}/n_O can be determined easily based on the following reaction scheme. Hence, once an n_O profile is parametrized, n_{O3} profile can be derived. Note that brackets [ ] in this section and the following sections represent number density of a certain species in units of $molecule$ per cm^3.

One of the famous hypotheses on ozone chemistry is proposed by Sydney Chapman in 1930. Molecular oxygen is firstly dissociated by solar radiation into atomic oxy-

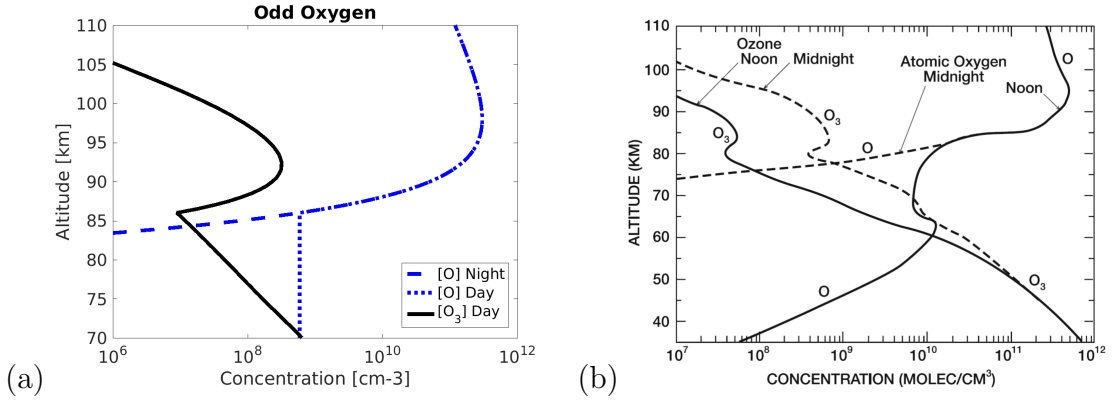

Figure 3.1: (a):The vertical profile of atomic oxygen concentration in the night (blue dashed line), according to the approximation in Eq 3.2 and values for parameters shown in Table 3.1, the atomic oxygen number density in the day (blue dotted line) modeled as Eq 3.3 and ozone number density in the day (black solid line) calculated from Eq 3.10 with solar zenith angle of 60 °. (b):The vertical concentration profiles for atomic oxygen and ozone calculated from the model of Garcia and Solomon (1983). Note that altitude ranges are different.

gen. These atoms may react with another oxygen molecule and a third body that stabilises the energy and momentum in the reaction to produce ozone. However, ozone can be destroyed by atomic oxygen as well as solar radiation. In this scheme, the sequence of reactions are

$$\mathrm{O_2} + h\nu \xrightarrow{J_{O2}} \mathrm{O} + \mathrm{O}, \tag{3.4}$$

$$\mathrm{O} + \mathrm{O_2} + \mathrm{M} \xrightarrow{k_a} \mathrm{O_3} + \mathrm{M}, \tag{3.5}$$

$$\mathrm{O_3} + \mathrm{O} \xrightarrow{k_b} 2\,\mathrm{O_2}, \tag{3.6}$$

$$\mathrm{O_3} + h\nu \xrightarrow{J_{O3}} \mathrm{O} + \mathrm{O_2}, \tag{3.7}$$

where J_{O2} and J_{O3} are the total photolysis rate of $\mathrm{O_2}$ and $\mathrm{O_3}$, respectively. k_a and k_b are the rate coefficients for corresponding reactions. M represents a third body, whose concentration can be assumed to be the sum of $[\mathrm{O_2}]$ and $[\mathrm{N_2}]$ in the homosphere. Following the reaction scheme above, the production rate and loss rate of ozone can be calculated as

$$\frac{d[\mathrm{O_3}]}{dt} = k_a[\mathrm{M}][\mathrm{O_2}][\mathrm{O}], \tag{3.8}$$

$$-\frac{d[\mathrm{O_3}]}{dt} = J_{\mathrm{O_3}}[\mathrm{O_3}] + k_b[\mathrm{O}][\mathrm{O_3}]. \tag{3.9}$$

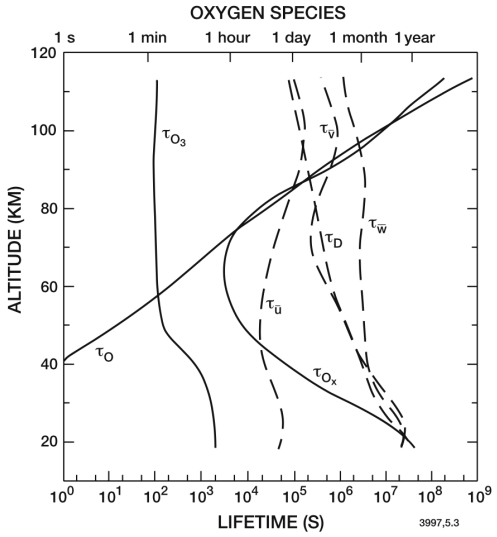

Figure 3.2: Altitude profiles of photochemical lifetimes of odd oxygen family Ox, O_3 and O. $\tau_{\bar{u}}$, $\tau_{\bar{v}}$ and $\tau_{\bar{w}}$ are the time constants for transports by the zonal, meridional and vertical winds at corresponding altitudes, respectively. τ_D is the one-dimensional vertical diffusive lifetime. Garcia and Solomon (1994)

Above the altitude of 70 km, atomic oxygen becomes more abundant in the odd oxygen family, because the reaction rate of Eq 3.5 become slower and Eq 3.7 become faster with increasing altitude. Ozone is no longer a long lived species in this region in comparison to those in the stratosphere and troposphere and atomic oxygen's lifetime becomes longer and longer with increasing altitude (Figure 3.2). Therefore, ozone can be considered in its photochemical equilibrium with atomic oxygen ($d[\mathrm{O_3}]/dt = -d[\mathrm{O_3}]/dt = 0$) and the concentration can be calculated as

$$[\mathrm{O_3}]^{day} = \frac{k_a[\mathrm{M}][\mathrm{O_2}][\mathrm{O}]^{day}}{J_{\mathrm{O_3}} + k_b[\mathrm{O}]^{day}}. \tag{3.10}$$

After sunsets, due to the lack of solar radiation, reactions in Eq 3.4 and Eq 3.7 stop to produce atomic oxygen. Because O_3, O_2 and N_2 are abundant in low altitudes, Eq 3.5 and Eq 3.6 remain to "eat up' atomic oxygen thus its number density drops rapidly in low altitudes. With the lack of atomic oxygen and sunlight, ozone is neither produced nor destroyed. Figure 3.1(b) shows vertical profiles of number density for atomic oxygen and ozone at noon and midnight calculated from a model of Garcia and Solomon (1983).

The above reaction scheme explains why different profiles of [O] for the day and the night are needed in the presented model. Pay attention that ozone has a lifetime of around 100s in the region of $70 - 110$ km, which is much shorter than periods of gravity waves under consideration in this thesis, 1h - 2h. Fluctuations driven by the gravity waves in [M], [O_2], [O] and temperature must be taken into account when modeling the ozone distribution. To calculate the nightglow emission field, ozone is not involved in the chemical processes to produce $\mathrm{O_2}(b^1\Sigma_g^+)$, which will be explained

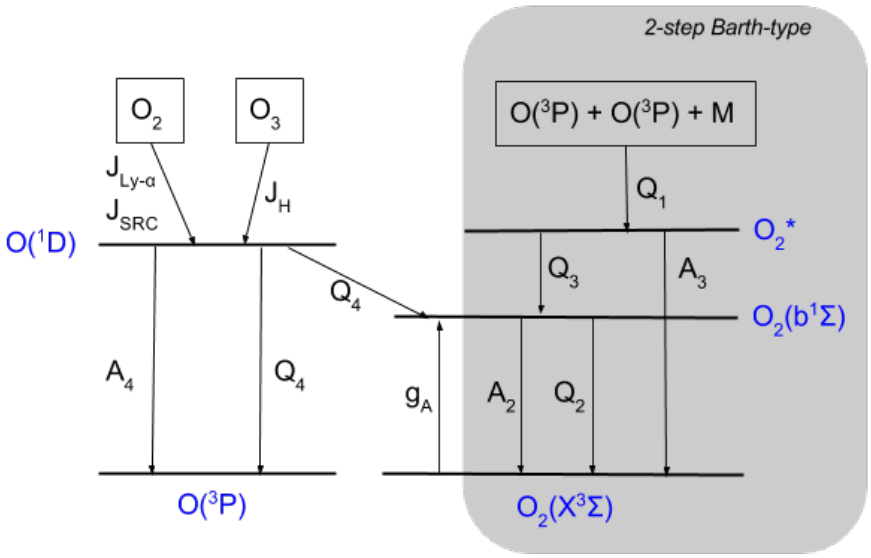

Figure 3.3: Processes that are accounted for the production of $O_2(b^1\Sigma_g^+)$ in the model. J and g terms represent photochemical reactions. Q terms represent collisional quenching. A terms represent the inverse photochemical lifetimes of the emitting states.

in the following section. Consequently, the ozone profile for the night $[O_3]^{night}$ is not needed to parametrized in this model. Figure 3.1(a) visualises vertical profile of $[O]^{night}$, $[O]^{day}$ and $[O_3]^{day}$ in an unperturbed state in this model.

3.3 $O_2(b^1\Sigma_g^+)$ production and loss

The photochemical processes governing the production and loss of $O_2(b^1\Sigma_g^+)$ must be understood before investigating how gravity waves affect the A-band airglow distributions.

During the day when the ultraviolet radiation from the sun hits oxygen molecules and ozone in the atmosphere, they are dissociate into individual oxygen atoms and electrons in each of these atoms jump into a higher orbital around their nuclei because of the extra energy they received. These individual excited oxygen atoms can either be further quenched into oxygen atoms in the ground state or help ground state oxygen molecules to become $O_2(b^1\Sigma_g^+)$. At the same time ground state oxygen molecules can also be excited by resonant absorption in the atmospheric band. Another mechanism to produce $O_2(b^1\Sigma_g^+)$ is by a 2-step Barth-type chemical reaction. This mechanism is initiated by a collision between two oxygen atoms and a third body to produce an unspecified excited oxygen molecule (O_2*). A ground state oxygen molecule can be a transfer agent to react with O_2* and produce $O_2(b^1\Sigma_g^+)$. Since the Barth-type chemical reaction dose not require absorption of sunlight, this is the only way to produce $O_2(b^1\Sigma_g^+)$ after the sunset. The overall mechanism for producing $O_2(b^1\Sigma_g^+)$ both in the day and the night is illustrated in Figure 3.3. The

detailed sequences of photochemistry reactions are divided into subsections namely: the Barth-type mechanism, quenching from O(^{1}D) and resonant absorption in A-band.

The Barth-type mechanism

Under the proposed transfer mechanism in McDade et al. (1986) and Murtagh et al. (1990), the sequence of reactions which will determine the the concentration of $O_2(b^1\Sigma_g^+)$ from 2-step Barth-type mechanism is presented in Eq 3.11 - 3.17

$$\mathrm{O + O + M} \xrightarrow{\alpha k_1} \mathrm{O_2{}^* + M}, \tag{3.11}$$

$$\mathrm{O_2{}^* + O_2} \xrightarrow{\gamma k_3{}^{\mathrm{O_2}}} \mathrm{O_2(b^1\Sigma_g^+) + O_2}, \tag{3.12}$$

$$\mathrm{O_2{}^* + O_2, N_2, O} \xrightarrow{k_3{}^{\mathrm{O_2,N_2,O}}} \mathrm{all\,products}, \tag{3.13}$$

$$\mathrm{O_2{}^*} \xrightarrow{A_3} \mathrm{O_2} + h\nu, \tag{3.14}$$

$$\mathrm{O_2(b^1\Sigma_g^+) + O_2, N_2, O} \xrightarrow{k_2{}^{\mathrm{O_2,N_2,O}}} \mathrm{quenched\,products}, \tag{3.15}$$

$$\mathrm{O_2(b^1\Sigma_g^+)} \xrightarrow{A_1} \mathrm{O_2(X)} + h\nu(\mathrm{O{-}O}), \tag{3.16}$$

$$\mathrm{O_2(b^1\Sigma_g^+)} \xrightarrow{A_2} \mathrm{O_2(X)} + h\nu(\mathrm{total}), \tag{3.17}$$

where α and γ represent the fraction of re-combinations into the unspecified excited state O_2* and from this state to $O_2(b^1\Sigma_g^+)$, respectively. k_1, k_2 and k_3 are the reaction rate coefficients for the collisions, marked as Q_1, Q_2 and Q_3 in Figure 3.3, respectively. A_1 is the Einstein A coefficient for the specific transition, from $O_2(b^1\Sigma_g^+)$ to ground state in this case, and A_2 and A_3 are the inverse photochemical lifetimes of the emitting states.

In photochemical equilibrium, the concentration of $O_2(b^1\Sigma_g^+)$ from the Barth-type mechanism can be calculated as

$$[\mathrm{O_2(b^1\Sigma_g^+)}]_{Barth} = \frac{\alpha k_1[\mathrm{O}]^2\,[\mathrm{M}]\,\gamma \mathrm{k_3}^{\mathrm{O_2}}\,[\mathrm{O_2}]}{\{Q_2 + A_2\}\cdot\{Q_3 + A_3\}}, \tag{3.18}$$

where

$$\begin{aligned} Q_2 &= k_2^{O_2}[\mathrm{O_2}] + k_2^{N_2}[\mathrm{N_2}] + k_2^{O}[\mathrm{O}], \\ Q_3 &= k_3^{O_2}[\mathrm{O_2}] + k_3^{N_2}[\mathrm{N_2}] + k_3^{O}[\mathrm{O}]. \end{aligned} \tag{3.19}$$

Table 3.2: Excitation parameters obtained by McDade et al. (1986)

	C^{O_2}	C^O
Interpolated [O] with:		
MSIS-83 and $k_2^O = 0$	7.5	33
MSIS-83 and $k_2^O = 8 \times 10^{-14}$	6.6	19
Interpolated [O] with:		
CIRA 1972 and $k_2^O = 0$	5.5	25
CIRA 1972 and $k_2^O = 8 \times 10^{-14}$	4.8	15

Because α, γ and k_3 are quantities that are often unknown, introducing empirical quenching coefficients can simplify the problem by fitting values from experiments. Since it is impossible to separate quenching by O_2 and N_2 from rocket measurements, it has to be assumed that $R = [N_2] : [O_2] \approx 4$. Eq 3.18 and Eq 3.19 can be then rewritten as

$$[O_2(b^1\Sigma_g^+)]_{Barth} = \frac{k_1[O]^2\,[M]\,[O_2]}{\{Q_2 + A_2\} \cdot \{C^{O_2}[O_2] + C^O[O]\}}, \tag{3.20}$$

where

$$\begin{aligned} C^{O_2} &= \frac{1 + Rk_3^{N_2}/k_3^{O_2}}{\alpha\gamma}, \\ C^O &= \frac{k_3^O/k_3^{O_2}}{\alpha\gamma}. \end{aligned} \tag{3.21}$$

The spontaneous emission from O_2*, A_3, has been dropped since it is often more difficult to obtain and not the dominate sink for O_2* in comparison to the collision (Murtagh (1995)). These newly introduced empirical quenching coefficients were evaluated by rocket measurements of nightglow emissions, using values of [O] given from either MSIS-83 and CIRA 1972 and 2 values from of k_2^O. The corresponding quenching coefficients are shown in Table 3.2. Values utilised in the current model are $C^{O_2} = 6.6$ and $C^O = 19$.

Quenching of O(^{1}D)

Another source of $O_2(b^1\Sigma_g^+)$ considered in this thesis is from the quenching of O(^{1}D), marked as Q_4 in Figure 3.3. Therefore, the concentration of O(^{1}D) must be determined before calculating $O_2(b^1\Sigma_g^+)$. There are two sources producing O(^{1}D): dissociation of ozone in the Hartley band, and dissociation of molecular oxygen in the Schumann-Runge continuum and $Ly-\alpha$ wavelengths. They are marked as J_H, J_{SRC} and $J_{ly-\alpha}$ in Figure 3.3, respectively. The sequence of chemical reactions is listed from Eq 3.22 to Eq 3.28 and detailed processes are described by Mlynczak et al. (1993),

$$O_3 + h\nu \xrightarrow{0.9J_H} O_2(^1\Delta) + O(^1D), \tag{3.22}$$

$$O_2 + h\nu \xrightarrow{J_{Ly-\alpha}} O(^3P) + O(^1D), \tag{3.23}$$

$$O_2 + h\nu \xrightarrow{J_{SRC}} O(^3P) + O(^1D), \tag{3.24}$$

$$O(^1D) + N_2 \xrightarrow{k_4^{N_2}} O(^3P) + N_2, \tag{3.25}$$

$$O(^1D) + O_2 \xrightarrow{0.77k_4^{O_2}} O(^3P) + O_2(b^1\Sigma_g^+), \tag{3.26}$$

$$O(^1D) + O_2 \xrightarrow{0.23k_4^{O_2}} O(^3P) + O_2, \tag{3.27}$$

$$O(^1D) \xrightarrow{A_4} O(^3P) + h\nu, \tag{3.28}$$

where k_4 are the rate coefficient for the quenching shown as Q_4 in Figure 3.3, A_4 is the inverse lifetime of $O(^1D)$.

In photochemical equilibrium, the concentration of $O(^1D)$ can be calculated as

$$[O(^1D)] = \frac{0.9J_H[O_3] + J_{Ly\alpha}[O_2] + J_{SRC}[O_2]}{A_4 + Q_4}, \tag{3.29}$$

where

$$Q_4 = k_4^{N_2}[N_2] + k_4^{O_2}[O_2]. \tag{3.30}$$

Reaction in Eq 3.26 becomes the source of producing $O_2(b^1\Sigma_g^+)$ from $O(^1D)$ while sinks for $O_2(b^1\Sigma_g^+)$ are the same as shown in the Barth-type mechanism. Thus, replacing $[O(^1D)]$ in Eq 3.29, the concentration of $O_2(b^1\Sigma_g^+)$ produced from $O(^1D)$ can be calculated as

$$\begin{aligned}[O_2(b^1\Sigma_g^+)]_{O(^1D)} &= \frac{0.77k_4^{O_2}[O_2][O(^1D)]}{A_2 + Q_2} \\ &= \frac{\{0.77k_4^{O_2}[O_2]\} \cdot \{0.9J_H[O_3] + J_{Ly\alpha}[O_2] + J_{SRC}[O_2]\}}{\{A_2 + Q_2\} \cdot \{A_4 + Q_4\}}.\end{aligned} \tag{3.31}$$

Resonant absorption in A-band

O_2 in the ground state can be also directly excited by the absorption of solar radiation at 762 nm (atmospheric A-band) to produce $O_2(b^1\Sigma_g^+)$,

$$O_2 + h\nu(762nm) \xrightarrow{g_A} + O_2(b^1\Sigma_g^+). \tag{3.32}$$

While the sinks for $O_2(b^1\Sigma_g^+)$ are still the same as shown in Barth-type mechanism $(A_2 + Q_2)$, the concentration can be calculated as

$$[O_2(b^1\Sigma_g^+)]_{g_A} = \frac{g_A[O_2]}{A_2 + Q_2}, \tag{3.33}$$

where g_A is the solar excitation rate at 762 nm.

Values for all reaction rate coefficients and inverse lifetimes used in the model are given in Table B.1 in the Appendix. Detailed calculations for the photolysis rates J_{O3}, J_H, $J_{ly-\alpha}$, J_{SRC} and solar excitation rate g_A will be further discussed in Section 3.4 and Section 3.5. Overall, by combining the three types of sources shown above with the presence of solar radiation, the concentration of $O_2(b^1\Sigma_g^+)$ during the day is modeled as

$$[O_2(b^1\Sigma_g^+)]^{day} = [O_2(b^1\Sigma_g^+)]_{Barth} + [O_2(b^1\Sigma_g^+)]_{O(^1D)} + [O_2(b^1\Sigma_g^+)]_{g_A}, \tag{3.34}$$

where the parametrized $[O]^{day}$ in Eq 3.3 and calculated $[O_3]^{day}$ in Eq 3.10 are used. Without solar radiation, the Barth-type mechanism is the only source to produce $O_2(b^1\Sigma_g^+)$, thus during the night the concentration is modeled as

$$[O_2(b^1\Sigma_g^+)]^{night} = [O_2(b^1\Sigma_g^+)]_{Barth}, \tag{3.35}$$

where the parametrized $[O]^{night}$ in Eq 3.2 is used.

3.4 The photolysis rates

Solar radiation is the main source of energy that is affecting photochemical processes which occurs in the middle atmosphere. To allow this energy reach to the Earth's surface, it has to penetrate the Earth's atmosphere. Various kinds of molecules in the atmosphere absorb the incoming solar flux in specific spectral region and use the extra energy to change their rotational, vibrational and electronic energy states. Since radiation of solar origin is in focus, the incoming solar flux and cross sections of molecules are taken in spectral region of $7.5 - 360\ nm$. Radiation of terrestrial origin is neglected here. Figure 3.5(a) shows the incoming flux spectrum utilised in the computation.

Following the Beer-Lambert law, radiative transfer model is presented as

$$J(\lambda, z) = J_o(\lambda) \cdot e^{-\tau(\lambda,z)}, \tag{3.36}$$

where λ represents wavelength and z is altitude. J and J_0 are the intensity of energy leaving the point in question and the intensity of energy before penetrating the atmosphere, respectively. τ is the optical depth, which is defined as

$$\tau(\lambda, z) = \sum_k [\sigma_k(\lambda) \cdot \sum_{z'} (n_k(z') \cdot dl(z, z'))], \tag{3.37}$$

where n_k represents the concentration of a specific absorbing species k, σ_k represents the cross sectional area of the species which is assumed not to be altitude dependent, i.e. independent from temperature. dl is the path length that the in coming flux has penetrated from the top of atmosphere reaching to the point in question through each atmospheric layer over head. Since path length dl is a function of altitude of the point in question z and the altitude of the atmospheric layer over head z', the following model is needed. Assuming the concentration is constant in the horizontal plane, i.e. absorbing species is equally distributed horizontally and n_k only depends on altitude of the atmospheric layer, the column number density is calculated as

$$\sum_{z'}[n_k(z') \cdot dl(z,z')] = \begin{bmatrix} n_k(z_1) & n_k(z_2) & n_k(z_3) & \dots & n_k(z_j) \end{bmatrix} \cdot \begin{bmatrix} l_{11} & 0 & 0 & \dots & 0 \\ l_{12} & l_{22} & 0 & \dots & 0 \\ l_{13} & l_{23} & l_{33} & \dots & 0 \\ \vdots & \vdots & \vdots & \ddots & \vdots \\ l_{1j} & l_{2j} & l_{3j} & \dots & l_{ij} \end{bmatrix}, \quad (3.38)$$

where the physical meaning of each component l_{ij} is the radiation path length through each atmospheric layer. Its relationship to the latitude z_i is illustrated in Figure 3.4. This 2nd order tensor can be computed according to the zenith angle of sunlight and the altitude interval dz. Depending the local time of the day, the solar zenith angle changes along the satellite measurements. Thus, the path length $dl(z)$ is also a function of solar zenith angle. The longest distance in the simulation domain in this thesis is along the y-direction, i.e. latitude direction, which is 1440 km. Although this will make about maximum 13° difference in solar zenith angle, it is considered to have minor influence in the calculation result of the 2nd order tensor l_{ij} when the solar zenith angle is low. For larger zenith angles, significant differences will occur and they should be avoided as one of the limitations of the model. Nevertheless, the solar zenith angle is assumed to independent from altitude, longitude and latitude through out the domain in the current model.

Since O, O_3, O_2 and N_2 have the major impacts on solar radiative transfer in this spectral region in terms of their mixing ratio above the altitude of 70 km, other minor constituents in the upper and middle atmosphere, such as water vapor, carbon dioxide and methane are neglect-able from absorbing the solar radiation. Hence, the optical depth in Eq 3.37 is calculated as

$$\begin{aligned} \tau(\lambda,z) = \sigma_O(\lambda) \cdot \sum_{z'}(n_O(z') \cdot dl(z,z')) \\ + \sigma_{O_3}(\lambda) \cdot \sum_{z'}(n_{O_3}(z') \cdot dl(z,z')) \\ + \sigma_{O_2}(\lambda) \cdot \sum_{z'}(n_{O_2}(z') \cdot dl(z,z')) \\ + \sigma_{N_2}(\lambda) \cdot \sum_{z'}(n_{N_2}(z') \cdot dl(z,z')). \end{aligned} \quad (3.39)$$

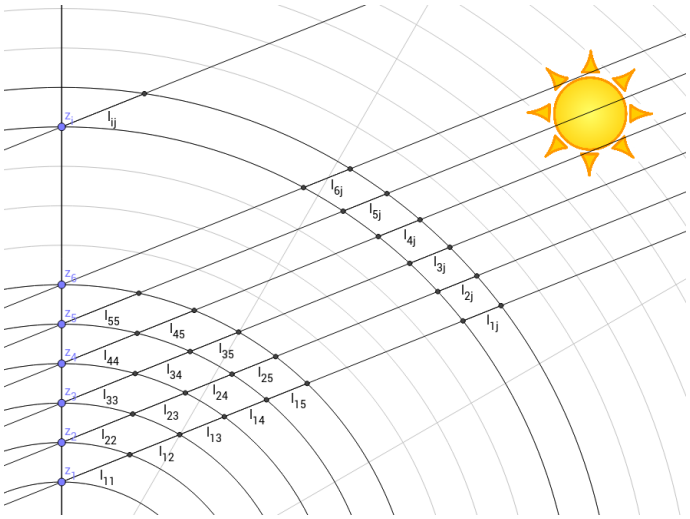

Figure 3.4: An illustration of the physical meaning of the 2nd order tensor l_{ij} in Eq 3.38.

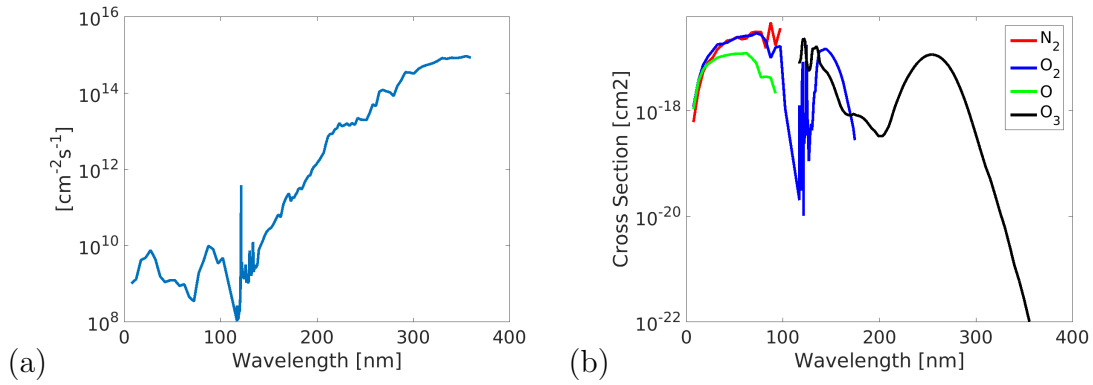

Figure 3.5: The incoming solar flux spectrum J_0 (a) and absorption cross sections spectra of O, O_3, O_2 and N_2 (b) utilised in the model.

where σ_O, σ_{O_3}, σ_{O_2} and σ_{N_2} are assumed to be independent from temperature and are taken from the HITRAN database Rothman et al. (2009). Absorption cross sections spectra of the four constituents are shown in Figure 3.5(b). Vertical concentration profiles n_O, n_{O_3}, n_{O_2} and n_{N_2} are taken from 70 km up to 150 km. Concentrations are assumed to be steady and horizontally uniform. In other words, τ is steady and horizontally uniform and zero above altitude of 150 km.

Finally, the dissociation rate of ozone photolysis in the Hartley band J_H, the dissociation rate of O_2 photolysis in the Schumann-Runge continuum J_{SRC} and $Ly - \alpha$

wavelengths $J_{ly-\alpha}$ are

$$\begin{aligned} J_H(z) &= \sum_{\lambda=210nm}^{310nm} \sigma_{O_3}(\lambda) \cdot J(\lambda, z), \\ J_{ly-\alpha}(z) &= \sigma_{O_2}(\lambda = 121.6nm) \cdot J(\lambda = 121.6nm, z), \\ J_{SRC}(z) &= \sum_{\lambda=112nm}^{175nm} \sigma_{O_2}(\lambda) \cdot J(\lambda, z). \end{aligned} \tag{3.40}$$

The total photolysis rates from O_3 and O_2 are

$$\begin{aligned} J_{O_3}(z) &= \sum_{\lambda=7.5nm}^{360nm} \sigma_{O_3}(\lambda) \cdot J(\lambda, z), \\ J_{O_2}(z) &= \sum_{\lambda=7.5nm}^{360nm} \sigma_{O_2}(\lambda) \cdot J(\lambda, z). \end{aligned} \tag{3.41}$$

3.5 The solar excitation rate in A-band

Unlike the calculation for the photolysis rates, where the absorption cross section σ is assumed to be temperature independent, the solar excitation rate in A-band g_A needs to consider the detail structure of the absorption band. The shape of the absorption lines is affected by Lorentz broadening and Doppler broadening. Lorentz broadening is the result of collisions between molecules and Doppler broadening is due to the thermal motion of molecules. Because the region in focus is in the upper mesosphere, Lorentz broadening is neglected here. In other words, the line shape function depends on temperature T and frequency ν (or wavelength λ). The absorption cross section of molecular oxygen in A-band is calculated using band strengths from the HITRAN spectroscopic database (Rothman et al. (2009)) as a product of spectral line strength S and Doppler line broadening g_D

$$\sigma_{O_2}(\nu, T) = \sum_{\nu_0} [S(\nu_0, T) \cdot g_D(\nu - \nu_0, T)], \tag{3.42}$$

where

$$g_D(\nu - \nu_0, T) = \sqrt{\frac{\ln 2}{\pi}} \frac{1}{\gamma_D} \exp[-(\frac{\ln 2(\nu - \nu_0)^2}{\gamma_D^2}]. \tag{3.43}$$

ν_0 is the midpoint of the line and γ_D indicates the half width of half maximum of the line. Such Doppler width is a function of T and ν_0

$$\gamma_D(\nu_0, T) = \frac{\nu_0}{c} \sqrt{\frac{2k_b T}{m_{O_2}}}, \tag{3.44}$$

where k_b is Boltzmann constant, m_{O_2} is molecule mass of O_2 and c is speed of light.

Such $S(\nu_0, T)$ in Eq 3.42 can be obtained from the HITRAN database, where a reference line strength $S_{298}(\nu_0)$ and the energy of the lower state $E''_{low}(\nu_0)$ are given

when $T = 298\ K$,

$$S(\nu_0, T) = S_{298}(\nu_0)\frac{T}{298}\exp[\frac{c_1 E''_{low}(\nu_0)\cdot(T-298)}{(298\cdot T)}], \tag{3.45}$$

where $c_1 = hc/k_b$ is the second radiation constant. h is the Plank's constant.

Finally, the optical depth τ is calculated as shown in Eq 3.37, taking a product of the path lengths and concentration of O_2 of all atmospheric layers

$$\tau(\nu, T) = \sigma_{O_2}(\nu, T)\cdot\sum_{z'}(n_{O_2}(z')\cdot dl(z, z')). \tag{3.46}$$

Solar excitation rate g_A is derived as

$$g_A(z) = \sum_{\nu}[\sigma_{O_2}(\nu, T)J_{762}\ e^{-\tau(\nu,T)}] \tag{3.47}$$

where J_{762} is solar irradiance J_0 at $\lambda = 762nm$, whose value is taken from World Meteorological Organization (WMO). Here, temperature T can be seen as a function of altitude z. The background temperature $\bar{T}(z)$ is utilized in the current model.

3.6 The spectra model derived from HITRAN

As already mentioned in Eq 1.2, the volume emission rate of airglow emitted from $O_2(b^1\Sigma_g^+)$ either in daytime or nighttime is calculated as

$$V_A = A_1\cdot[O_2(b^1\Sigma_g^+)] \tag{3.48}$$

where the adopted Einstein A coefficient A_1 can be found in Table B.1. The field of airglow intensity has a unit of $[photons\ cm^{-3}\ s^{-1}]$. The calculated values for V_A represent the total emission brightness over the entire A-band vibrational transition spectrum. They need to be filtered down to two selected spectral bands, namely IR channel 1 ($759 - 767\ nm$) and IR channel 2 (around $760 - 764\ nm$) according to the preliminary design of MATS instrument. Spectral analysis is the basis for the atmospheric temperature retrieval. The brightness of the corresponding channel can be related to a calculated value from a spectra model at A-band. Here, HITRAN spectroscopic database (Rothman et al. (2009)) was used to derive such spectra model, given temperatures between $100 - 300\ K$ at $1\ K$ intervals and spectral lines between $758 - 770\ nm$ with $2\times10^{-4}\ nm$ spectral resolution. Examples are shown in Figure 3.6 for temperatures in $100\ K$, $200\ K$ and $300\ K$. By integrating the line strengths over the entire spectrum, as well as the selected spectral regions for the channels, normalised emission intensities of channel 1 and channel 2 are computed as functions of temperature

$$\begin{aligned} E_1^{norm}(T) &= E_{tot}^{-1}\sum_{\lambda=759}^{767} I(\lambda, T); \\ E_2^{norm}(T) &= E_{tot}^{-1}\sum_{\lambda=760}^{764} I(\lambda, T), \end{aligned} \tag{3.49}$$

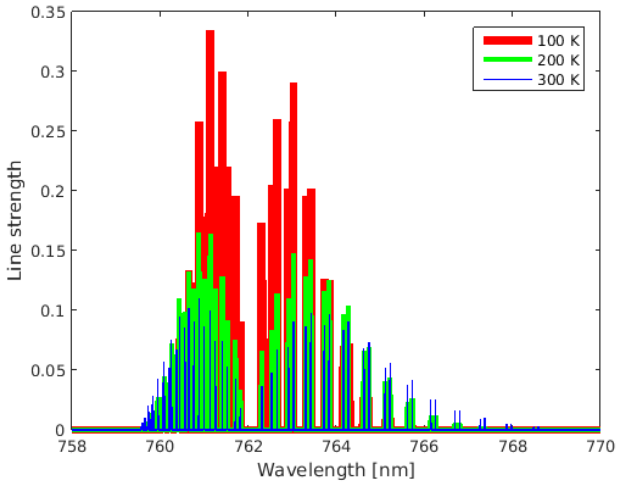

Figure 3.6: The spectra model derived from HITRAN database at $T = 100, 200, 300\ K$

where

$$E_{tot} = \sum_{\lambda=758}^{770} I(\lambda, T). \tag{3.50}$$

Finally, airglow emission rates as functions of 3 spatial dimensions and time for each channel are calculated as

$$\begin{aligned} V_1(x, y, z, t) &= V_A(x, y, z, t)\ E_1^{norm}(T_l); \\ V_2(x, y, z, t) &= V_A(x, y, z, t)\ E_2^{norm}(T_l), \end{aligned} \tag{3.51}$$

where T_l is the temperature at the corresponding location and time, thus it is also a function of 3 spatial dimensions and time $T_l(x, y, z, t)$.

4

Projection onto the image plane

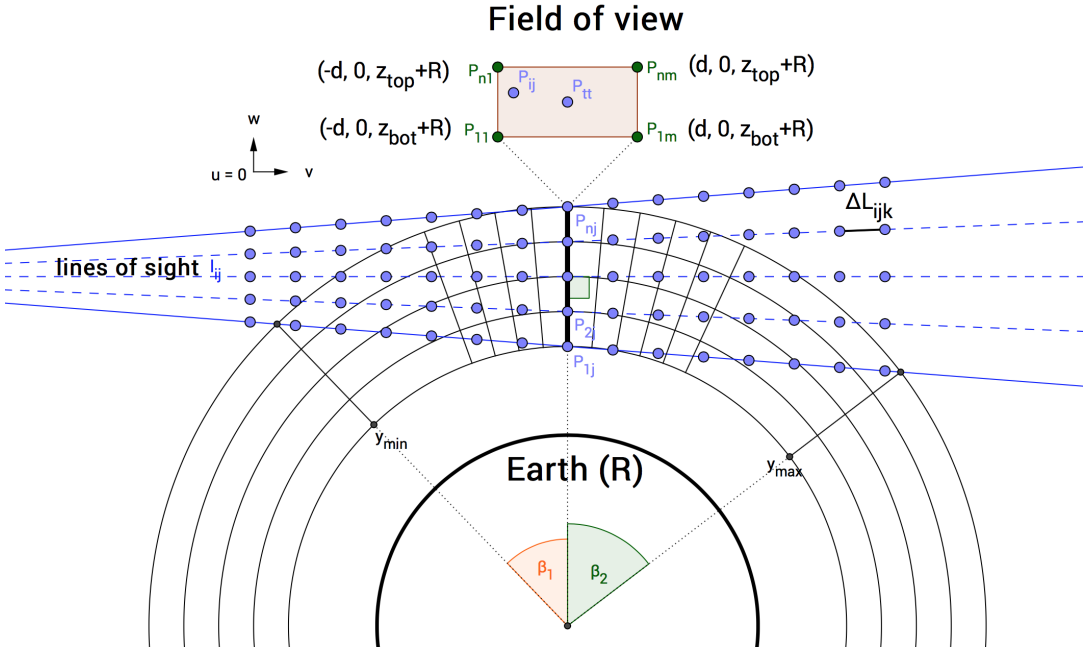

Figure 4.1: Observation geometry for the calculation of minimum requirements of domain size and the assumption made for calculation of limb radiance V_{ij} in Eq 4.7. Blue points represent points $\mathbf{X}_{ijk}$ on lines of sight l_{ij} that are used as query points when interpolation is made. Although it should be in a 3 dimensional space, this figure only illustrates viewing geometry in a 2 dimensional perspective on the $v-w$ plane with $u=0$. The red rectangular polygon is an exception which is on the $u-w$ plane. All lines of sight should intersect with the rectangular polygon.

The simulation domain and resolution must be large and high enough to cover the area where the imagers on board will observe. Because of the atmospheric sphericity, the limb-viewing geometry of the MATS satellite needs to be modeled. Consider in a geocentric reference system with three-dimensions along the Cartesian u, v and w axes, where u, v and w represent distance across the track from the orbit plane, distance from the tangent point on the orbit plane and distance from the center of the Earth. Assuming MATS is located at an orbit in an altitude of z_s and the center line-of-sight from the limb imaging instrument is align with the

tangent line at a point on the sphere in an altitude of z_{tan}, this tangent point can be defined as $\mathbf{P}_{tt} : (0, 0, z_{tan} + R)$ and the position of satellite can be $\mathbf{S} : (0, -\sqrt{(z_s + R)^2 - (z_{tan} + R)^2}, z_{tan} + R)$ in the Cartesian (u, v, w) coordinate, where R is the radius of the Earth. An illustration of the viewing geometry of MATS is shown in Figure 4.1. The horizontal limb field of view is $\pm d$ and vertical limb field of view is $z_{bot} - z_{top}$ in altitude, so that the tangent intersect area with the atmosphere can be seen as a rectangular polygon on the u-w plane. All observation lines of sight should cross any given point $\mathbf{P}_{ij} : (p_i, 0, p_j)$ on the rectangular polygon, where $-d < p_i < d$ and $z_{bot} + R < p_j < z_{top} + R$. These observation lines of sight can be described as a vector equation

$$\mathbf{l}_{ij} : \mathbf{X}_{ijk} = \mathbf{S} + k(\mathbf{P}_{ij} - \mathbf{S}), \tag{4.1}$$

where k is a scaling factor. $\mathbf{X}_{ijk}$ is any point on a given line-of-sight $\mathbf{l}_{ij}$. When $k = 0$, $\mathbf{X}_{ijk} = \mathbf{P}_{ij}$. Consequently, each vector component of $\mathbf{X}_{ijk}$ can be written as

$$\begin{aligned} X_{ijk}(u) &= S(u) + k(P_{ij}(u) - S(u)), \\ X_{ijk}(v) &= S(v) + k(P_{ij}(v) - S(v)), \\ X_{ijk}(w) &= S(w) + k(P_{ij}(w) - S(w)). \end{aligned} \tag{4.2}$$

Alternatively, $\mathbf{X}_{ijk}$ can be also described in a geocentric spherical coordinate system (α, β, ρ), where the conversion relation between this spherical system and the Cartesian system (u, v, w) (Figure 4.2) is

$$\begin{aligned} \alpha &= tan^{-1}(u/w), \\ \beta &= tan^{-1}(v/w), \\ \rho^2 &= u^2 + v^2 + w^2. \end{aligned} \tag{4.3}$$

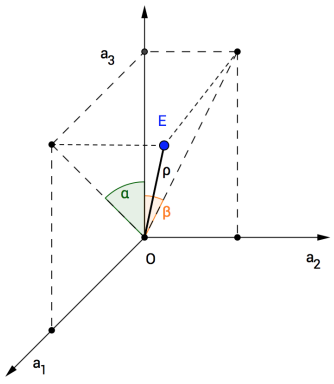

Figure 4.2: Coordinate conversion relation between the spherical system (α, β, ρ) and the Cartesian system (u, v, w).

On the other hand, a Cartesian coordinate system in three dimensions with x, y and z components is considered when simulating airglow distributions induced by

gravity waves. Components x and y represent the horizontal distances on a surface and z represent the vertical distance from a reference surface. Here, the reference surface is the Earth's surface, so that z is equivalent to the altitude. The minimum requirement for the range of these three components depends on the altitude of MATS satellite orbit z_s, the altitude region of the atmosphere under investigation z_{bot} and z_{top} and the horizontal field of view d. A conversion between coordinate systems (x, y, z) and (α, β, ρ) is shown as

$$\begin{aligned} x &= \alpha\ (R + 90) \\ y &= \beta\ (R + 90) \\ z &= \rho - R \end{aligned} \tag{4.4}$$

Assume the bottom and top limit of the atmosphere under investigation are same as the vertical limb field of view, which can be expressed in vector equations

$$\begin{aligned} \mathbf{c}_{bot} : \begin{bmatrix} u \\ v \\ w \end{bmatrix} &= (z_{bot} + R) \begin{bmatrix} sin(\alpha) \\ sin(\beta) \\ cos(\beta) \end{bmatrix}, \\ \mathbf{c}_{top} : \begin{bmatrix} u \\ v \\ w \end{bmatrix} &= (z_{top} + R) \begin{bmatrix} sin(\alpha) \\ sin(\beta) \\ cos(\beta) \end{bmatrix}. \end{aligned} \tag{4.5}$$

Consequently, z_{bot} and z_{top} will be the minimum requirement for the range of altitude z in the simulation domain.

Three lines of sight $\mathbf{l}_{11}$, $\mathbf{l}_{1t}$ and $\mathbf{l}_{1m}$ which cross $\mathbf{P}_{11} : (-d, 0, z_{bot}+R)$, $\mathbf{P}_{1t} : (0, 0, z_{bot}+R)$ and $\mathbf{P}_{1m} : (d, 0, z_{bot} + R)$, respectively, will intersect with $\mathbf{c}_{top}$ at 2 points each. The coordinates of these 6 points can be derived by solving system equations Eq 4.2 and Eq 4.5. Assume $\mathbf{X}_{11a}$ and $\mathbf{X}_{11b}$ are the points of intersection of the line $\mathbf{l}_{11}$ and the surface $\mathbf{c}_{top}$; $\mathbf{X}_{1ta}$ and $\mathbf{X}_{1tb}$ are the points of intersection of the line $\mathbf{l}_{1t}$ and the surface $\mathbf{c}_{top}$; $\mathbf{X}_{1ma}$ and $\mathbf{X}_{1mb}$ are the points of intersection of the line $\mathbf{l}_{1m}$ and the surface $\mathbf{c}_{top}$. Their coordinates in geocentric spherical reference system are

$$\begin{aligned} \mathbf{X}_{11a} : (-\alpha', \beta_1', z_{top} + R),\ \mathbf{X}_{11b} : (-\alpha, \beta_2', z_{top} + R), \\ \mathbf{X}_{1ta} : (0, \beta_1, z_{top} + R),\ \mathbf{X}_{1tb} : (0, \beta_2, z_{top} + R), \\ \mathbf{X}_{1na} : (\alpha', \beta_1', z_{top} + R),\ \mathbf{X}_{1nb} : (\alpha, \beta_2', z_{top} + R). \end{aligned} \tag{4.6}$$

The minimum requirements for simulation domain size in horizontal directions can be derived from α, β_1 and β_2 by using Eq 4.4. The corresponding values of k for point $\mathbf{X}_{1ta}$ and $\mathbf{X}_{1tb}$ in Eq 4.2, k_a and k_b, respectively, will be the minimum range requirement for the summation index k in Eq 4.7.

When an emission intensity profile $\mathbf{V}$ is computed from the simulation, values located at $\mathbf{X}_{ijk}$ need to be integrated along each observation line of sight $\mathbf{l}_{ij}$ as

$$V_{ij} = \sum_{k=a}^{b} [\mathbf{V}(\mathbf{X}_{ijk})\ \Delta L_{ijk}], \tag{4.7}$$

where ΔL_{ijk} represents the distance between two neighbouring points along the same line of sight, $\mathbf{X}_{ijk}$ and $\mathbf{X}_{ijk+1}$. V_{ij} is the limb radiance located at the ijth pixel on a so-called 'simulated satellite image' - an image has $i \times j$ pixels with i columns and j rows. Here, the region above z_{top} and below z_{bot} is assumed to be completely dark, i.e. $\mathbf{V} = 0$.

To find values of $\mathbf{V}$ located at each specific point of $\mathbf{X}_{ijk}$, interpolation must be performed. Considering the limitation of computation memory, the 'nearest' interpolation method is chosen. Problems might occur when query points $\mathbf{X}_{ijk}$ are not dense enough, i.e. ΔL_{ijk} are not short enough. To make sure ΔL_{ijk} is at least shorter than the simulation grid size for $\mathbf{V}$, iteration steps of 300 is chosen which corresponds to $\Delta L_{ijk} \approx 4.9\ km$. The simulated emission profile $\mathbf{V}$ is gridded data using (x, y, z) reference system while query points $\mathbf{X}_{ijk}$ are obtained in geocentric reference system (u, v, w). Either of them need to be converted to the same coordinate system with the other in order to perform interpolation. Figure 4.3 shows how all query points $\mathbf{X}_{ijk}$ along observation lines of sight look like in the (x, y, z) coordinate system.

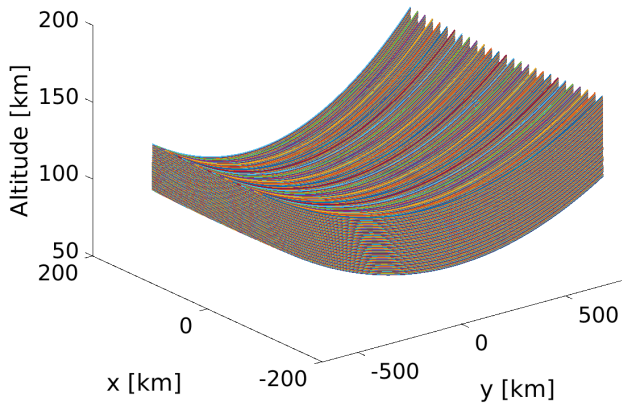

Figure 4.3: All query points $\mathbf{X}_{ijk}$ on observation lines of sight l_{ijk} are converted in Cartesian coordinate (x, y, z), the same coordinate system used in the simulation of emission intensity profile $\mathbf{V}$.

In this thesis, the following parameters of the observation geometry are adopted: $z_s = 600\ km$, $z_{bot} = 70\ km$, $z_{top} = 110$, $z_{tan} = (z_{bot} + z_{top})/2$ and $d = 130\ km$. By solving system equations Eq 4.2 and Eq 4.5, the solution for Eq 4.6 are given as $\alpha = 1.67°$, $\beta_1 = -5.95°$, $\beta_2 = 6.82°$, and the corresponding values for k are $k_a = 0.74$ and $k_b = 1.29$. Hence, the minimum requirement of the simulation domain size x, y, z and the minimum range of summation index k for obtaining airglow emission profile $\mathbf{V}$ are set. The simulation domain size in this thesis is slightly larger than the minimum requirements, as shown in Table 4.1.

Table 4.1: Summary of the simulation domain size and resolution for obtaining airglow emission profile $\mathbf{V}(x, y, z, t)$. k is a scaling factor for finding the point location at $\mathbf{X}_{ijk}$ along the line-of-sight, see Eq 4.2. It is also a summation index to calculate the total limb radiance along the line-of-sight.

Symbol	Physical meaning	Range	Resolution/steps
k	scaling factor	0.74 to 1.3	300 steps
x	across track distance	-200 to 200 km	4 km
y	along track distance	-670 to 770 km	10 km
z	altitude	70 to 110 km	0.5 km
t	time	0 to 1 wave period	10 steps

5

Model results

The main results from the model will be shown in this Chapter. Before the investigation on the influences from the gravity waves, the distributions of the dayglow emissions must be verified by comparing with other photochemistry models. Airglow fields perturbed by a gravity wave will then be investigated by adding perturbations in the temperature and number densities of atmospheric components. Simulated satellite images will then be shown, so that the wave characteristics projected onto the imager on board the satellite can be estimated. The limb images are treated as the 'final output' of the forward model and can be used for different purposes in the MATS project.

5.1 Airglow emission field

The unperturbed state

Generally speaking, it is considered to be day on the surface of the Earth when zenith solar angle is less than 90° , otherwise it is considered night. However, since the observation region is $70 - 100$ km above the Earth's surface, solar radiation can reach to this entire region up to zenith solar angle of 98.5°. Between 98.5° and 100.6° geometrical shading by the earth needs to be considered. Thus, the airglow model is defined as dayglow if solar zenith angle is less than 100.6°, otherwise it is nightglow. Hence, the background state of atomic oxygen concentration profile is parametrized differently according to the given solar zenith angle, either $[O]^{day}$ or $[O]^{night}$ as described in Section 3.1. The ozone concentration profile in the day $[O_3]^{day}$ is calculated from $[O]^{day}$, [M], $[O_2]$ and the corresponding reaction coefficients in the unperturbed state as described in Section 3.2. Based on the mechanisms of $O_2(b^1\Sigma_g^+)$ production and loss presented in Section 3.3, the vertical profile of the A-band airglow emission rate in the unperturbed state is computed.

Figure 5.1 shows the total dayglow and nightglow volume emission rates as well as different sources of the emission rates in the unperturbed state. Figure 5.1(a) is consistent with other O_2 A-band dayglow results from models presented in Sheese et al. (2010) and Mlynczak and Olander (1995). During the day, 4 major sources to the total concentration of $O_2(b^1\Sigma_g^+)$ can be identified clearly. They are: the Barth-

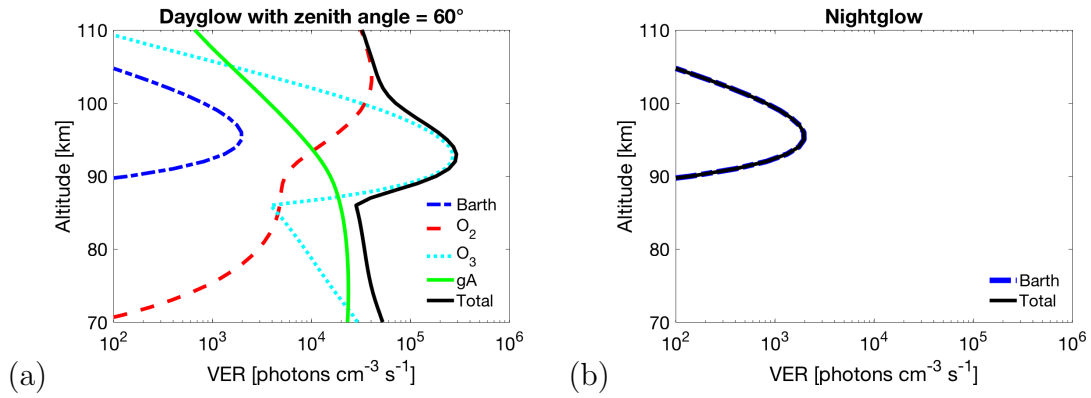

Figure 5.1: (a): The total volume emission rate (black solid line) of dayglow with solar zenith angle of 60° and its different sources. The blue dash-dotted line marked as 'Barth' represents the contribution from the Barth-type reaction. The red dashed line marked as O_2 and the cyan dotted line marked as O_3 are the contributions from $O(^1D)$ produced by photolysis of O_2 and O_3, respectively. The green solid line is the contribution from resonant absorption in A-band. (b): The total volume emission rate of nightglow and its only source from the Barth-type reaction, which is completely overlaid by the total emission profile. Note that the horizontal axis is log-scale in (a) but linear-scale in (b).

type three-body collision (O + O + M), collisions between the ground state O_2 and $O(^1D)$ which was produced in the photolysis of either O_2 or, O_3, and finally O_2 resonant absorption in A-band. The main contribution in the region above 98 km is from the collisional excitation with $O(^1D)$ that is produced from photolysis of O_2, while in the region between $88 - 98$ km is from photolysis of O_3. Below 88 km resonant scattering plays an important role for the total emission rate. Peak dayglow emission appears at the altitude of 93 km and the peak emission rate is highly sensitive to how much ozone is available in this region to be disassociated by the sunlight. Since the ozone concentration was calculated from the atomic oxygen concentration, the distribution of ozone highly depends on how the atomic oxygen profile was parametrized and modified in Eq 3.10 for daytime. On one hand, the Barth-type mechanism contributes to the total emission in the day to a significantly lesser extent in comparison to the other sources. On the other hand, total nightglow emission profile completely overlies with the Barth-type mechanism profile, which verifies that this mechanism is the only source to produce $O_2(b^1\Sigma_g^+)$ after sunsets. The peak value appears at 95 km and the rate of peak emission of nightglow is again highly sensitive to the parametrization of the atomic oxygen concentration. Nevertheless, the total emission rates from dayglow and nightglow are consistent with measurements data from OSIRIS. It is worth to mention that the horizontal scales are different by orders of magnitude between the day and the night.

Path lengths for the incoming solar flux vary with the increasing solar zenith angle in the day. Figure 5.2 shows how the total emission rates for the dayglow vary with different zenith angles, as well as their corresponding sources calculated from the photochemistry model. With no surprise, the contribution from the Barth-

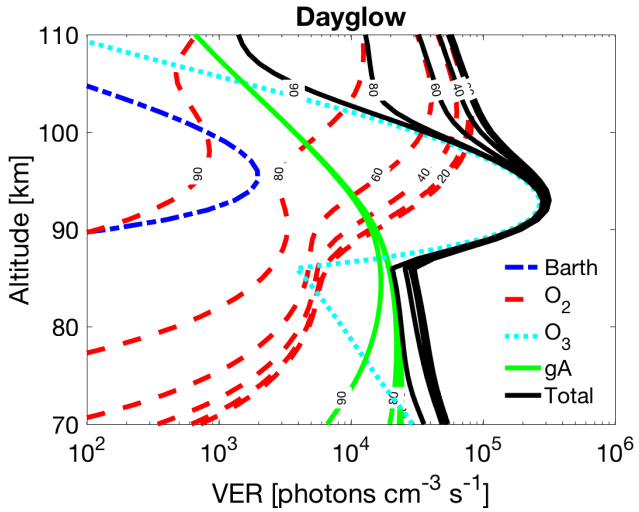

Figure 5.2: Same to Figure 5.1(a) but with solar zenith angle of 0°, 20°, 40°, 60°, 80° and 90°.

type reaction does not change with solar angle since photolysis is not involved here. Both resonant absorption of O_2 in A-band and photolysis of O_2 for $O(^1D)$ production decrease with increasing solar zenith angle. However, changes in the photolysis of O_3 for $O(^1D)$ production were too small to be identify in this figure. This is mainly due to that the parametrization of the atomic oxygen concentration in the day $[O]^{day}$ does not relate to the changing path lengths in the current model. As stated in the earlier paragraphs, background [O] was parametrized in two discrete states, either $[O]^{day}$ or $[O]^{night}$ depending on whether solar zenith angle was less or greater than 100.6°. In fact, there should be a smooth transition from $[O]^{day}$ to $[O]^{night}$ with increasing solar zenith angle. Because of the lack of observation data and knowledge of the atomic oxygen distribution in this atmospheric region, the transition from day to night was neglected and simplified in this model. Although calculations of dayglow emissions from O_3 involve J_H and $[O_3]^{day}$ where J_{O_3} computation is involved, the differences made in the photolysis rate computations with various solar angles were not significant enough to show changes in $O(^1D)$ production rates. As a result, the peak of the total dayglow emission almost remain constant.

The perturbed state

Airglow emission fields in perturbed state were computed when fluctuations occur on background temperature and number density of N_2, O_2, O, O_3 induced by gravity waves. Figure 5.3 shows vertical profiles of the total emissions at $x = y = t = 0$, as well as the emission fields in three dimensional space from day- or nightglow at an instant time $t = 0$. Wave parameters were set the same as those in Figure 2.3. It was shown that significant perturbations occur at around 88 ± 5 km and 97 ± 2.5 km altitude in the day, whereas 94 $km \pm 5$ altitude in the night. This implies that the imager on-board MATS can more easily to capture the characteristics of the wave in these regions according to the time of the day. Below 85 km and above 105 km

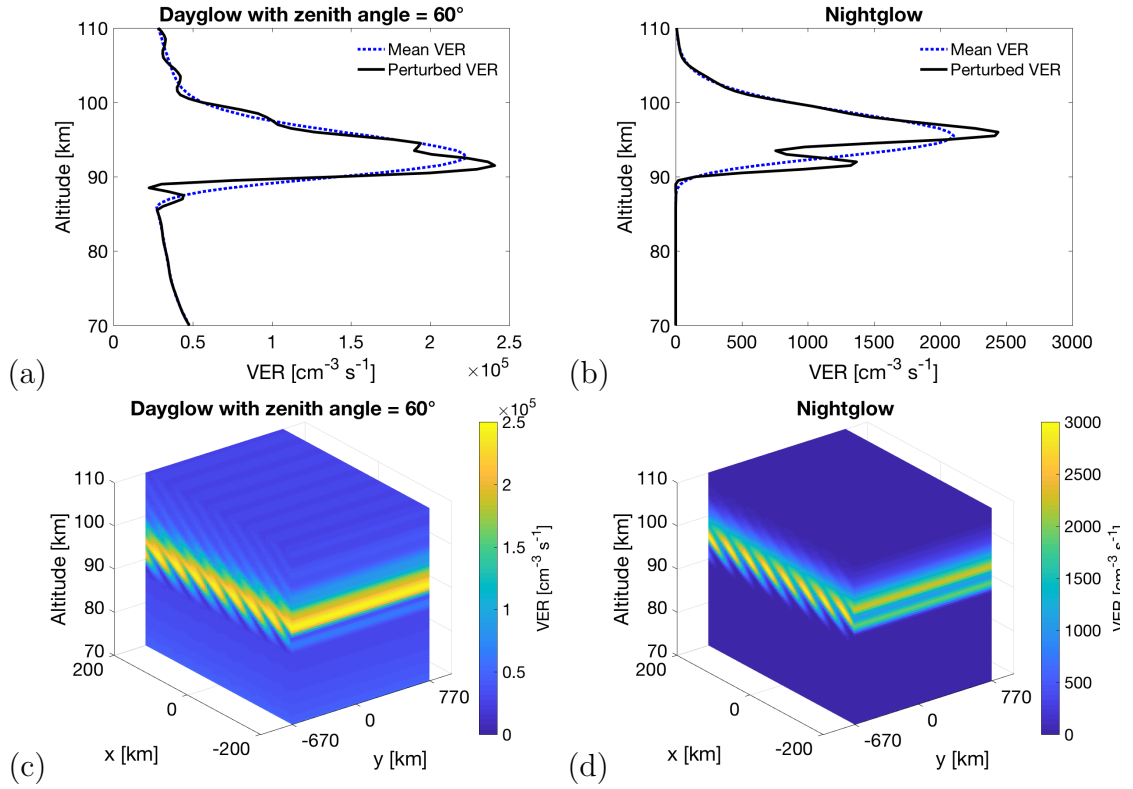

Figure 5.3: The airglow emissions perturbed by an internal gravity wave with wave period $2\pi/\omega = 1\ hour$, vertical wavelength $2\pi/k_z = 5\ km$, horizontal wavelength $2\pi/k_h \approx 52\ km$ with $\xi = 0$, reduced amplitude $A = 1\ km\ s^2$. The background state vertical profiles of the temperature and the bulk number density are taken from MSIS-90 model at latitude of 0 in June. The background state atomic oxygen profile is parametrized according to Eq 3.2 and Table B.2. Note that horizontal scales and color scales for the day- and nightglow are different. (a): The vertical profile of dayglow volume emission rate (VER) at $x = y = 0$. (b):Same to (a) but nightglow. (c): The dayglow VER field in three dimensions in the unit of $[photons\ cm^{-3}s^{-1}]$. (d):Same to (c) but nightglow.

altitude, perturbations are significantly smaller. The nightglow perturbations at around $94 - 95\ km$ and the dayglow perturbations at around $88\ km$ are as large as 50%.

5.2 Limb images

Using the measurement geometry and the spectral selections of MATS as described in the preliminary design report, the Earth's limb images are generated. Images contain 81×27 pixels, which represent the horizontal field of view range $\pm 130\ km$ and the vertical field of view $70 - 110\ km$. Values of the limb radiance calculated from Eq 4.7 are stored in the corresponding pixel and separated into two spectral channels, namely, Ch1 $(759 - 767nm)$ and Ch2 $(760 - 764nm)$. Figure 5.4 shows the

limb images in Ch1 and Ch2 of nightglow. As expected, the limb radiance strength in Ch2 is weaker than in Ch1. The left panel shows how the imager on MATS will observe when the horizontal phase front is parallel to the limb-viewing direction of MATS, i.e. $\xi = 0$ or $\xi = 180$, while the images on the right panel are when $\xi = 90°$ or $\xi = 270°$. The associated wave parameters and the nightglow emission field in three dimensional space can be found in Figure 5.3(d) for $\xi = 0$. The peaks of limb radiance intensities match the altitude range shown in Figure 5.3(b) and the curve line of the atmosphere is projected. The nightglow fluctuations occur the largest between 90 and 100 km or below 85 km when $\xi = 0$ or $\xi = 90°$, respectively. The images of the dayglow also show similar patterns. As expected, both the horizontal and the vertical wavelengths of the gravity wave are the best captured when the horizontal propagation direction is perpendicular to the track of MATS. While only half of the vertical wavelength (≈ 3 km) of the gravity wave can be seen when $\xi = 90°$. This implies that a tomographic reconstruction is needed, so that all wave characteristics can be estimated. Figure 5.5 shows five lines of sight passing through the nightglow emission field on the $y - z$ plane at $x = t = 0$. All lines of sight reach their lowest altitude at their individual tangent point, e.g. the line-of-sight crossing the tangent altitude of 90 km reaches its lowest point at $y = 0$. On one hand, when $\xi = 0$, the lines crossing tangent altitude above 100 and below 90 km either not cross the airglow layer or cross the entire airglow layer, thus the fluctuations are not obviously visible from the imager above 100 or below 90 km tangent altitude. On the other hand, when $\xi = 90°$, the lines of sight which cross below 85 km tangent altitude partly co-aligned along the sloping phase front of the gravity wave at around $y = 300 - 600$ km. Thus, the larger fluctuations can be observed from the imager below 85 km tangent altitude.

To summarise, wave characteristics are the best projected on the limb images when $\xi = 0$. When the orientation of the horizontal phase front ξ is unknown, a tomographic reconstruction or a more sophisticated retrieval algorithm which involves weighting functions for all the lines of sight is needed.

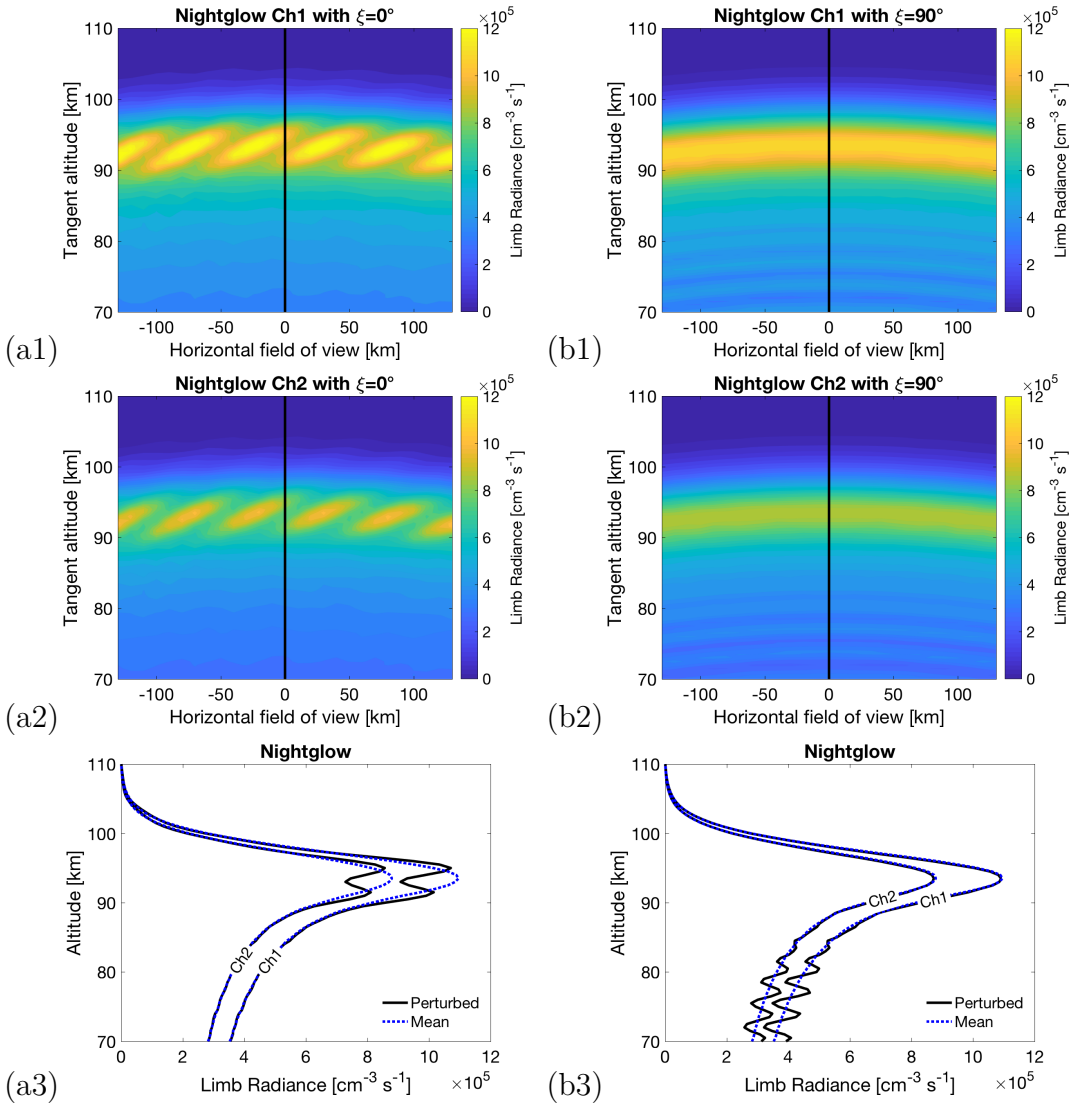

Figure 5.4: The simulated satellite images of nightglow in Ch1 and Ch2 when the horizontal propagation direction of the gravity wave is perpendicular (a) and parallel (b) to the limb-viewing direction of MATS. Values on colors represent the limb radiance. The bottom panel shows 1D-profiles along the center lines in the images indicated as black lines.

(a)

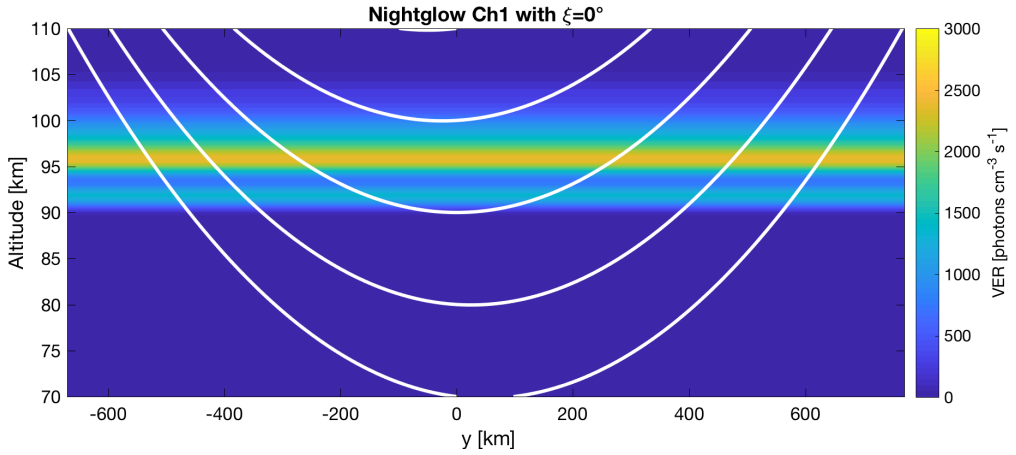

(b)

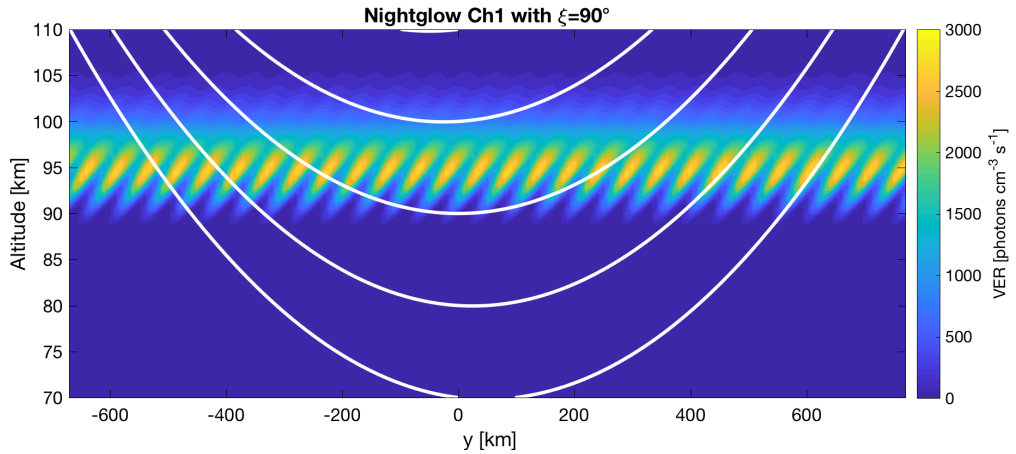

Figure 5.5: Five lines of sight crossing the tangent altitude of 70, 80, 90, 100 and 110 km. The background contour is the nightglow emission field in Ch1 on the $y-z$ plane at $x = t = 0$. The wave parameters are the same as shown in Figure 5.3 with $\xi = 0$ (a) and $\xi = 90°$ (b).

6

Conclusion

A three dimensional gravity wave model and an associated photochemistry model for A-band emission rates were implemented. They were coupled to simulate the perturbed O_2 nightglow emissions and dayglow emissions fields in three spacial dimensions and time. The simulated satellite images were then generated according to the limb-viewing geometry and the spectral selections for MATS as described in the preliminary design of the instrument. These images can indicate how MATS will observe airglow emission brightness with gravity waves present.

It was found that the wave characteristics are the easiest to captured between $85 - 105\ km$ tangent altitude when the horizontal phase front of the wave is parallel to the satellite orbit, due to the relatively large fluctuations in emission intensities. However, wave patterns are not obviously visible on the satellite images when the orientation of the horizontal phase front is perpendicular to the viewing direction of MATS. In such case, a tomographic reconstruction is necessary to retrieve the structure of gravity waves. Furthermore, it was shown that the airglow emission rates are highly sensitive to the background fields of the atomic oxygen and the ozone concentrations. Therefore, airglow measurements could possibly be used to derive these quantities.

Although the forward model is useful for further developments of the MATS project and other studies on atmospheric science, there are a few limitations and areas for improvement. A standing satellite is assumed in the current model, so that the size of domain for airglow emissions field is restricted due to the limited computational resources. In fact, MATS will be constantly moving with the speed of $7.5 km/s$. When the satellite is moving, the Doppler effect on the wave characteristics need to be taken account in the observation. To model a moving satellite, much longer range of the domain along the track, or a more effective algorithm is needed to save the limited computational resources.

The discrete input for number densities of atomic oxygen n_O is an important limitation in the photochemistry model. As discussed in Section 5.1, the atomic oxygen profile in the background state was parametrised as either n_O^{day} or n_O^{night} based on a solar angle threshold (zenith 110.6°), in order to separate computation processes of the dayglow and nightglow. Bias will be large in the total emission rate of dayglow when the solar zenith angle is large towards nightfall. There should be a smooth transition from n_O^{day} to n_O^{night}. Because of the lack of knowledge about atomic oxygen

concentrations in the region of $70 - 110\ km$ altitude, n_O is difficult to parametrised to how the actual situation look like. Improvement can be made when a more comprehensive model of atomic oxygen concentration is coupled to the photochemistry model, as well as more measurement data of n_O in this region to verify the accuracy of the model. Consequently, the accuracy of dayglow emissions can be improved as well since $[O_2(b^1\Sigma_b^+)]$ in the day involves computation of $n_{O_3}^{day}$ which was also calculated from n_O^{day}.

Another limitation comes from the assumption of the same solar zenith angle through out the simulation domain and the time period. In fact, solar angle can be up to 13° different since the longest distance is 1440 km in the y dimension, i.e. the viewing direction of the imager. This will make bias in the calculation result of the photolysis rates J and solar excitation rate in A-band g_A, especially when solar zenith angle is large towards nightfall. Improvement can be made by calculating solar angle for each location in the domain. Also, horizontal fluctuations in atmospheric components induced by gravity waves can be computed, instead of assuming horizontally uniformed. As a result, much higher computation costs are needed.

Other improvement areas exist in the gravity wave model. The model is monochromatic, which means only single wavenumber or frequency is assumed on each dimension, k_x, k_y, $_z$ and ω. In the actual atmosphere, several different wavenumbers and frequencies can exit at the same time. Also, the background wind is assumed to be zero in the current model. Possible extensions would be adding background wind from meridional and zonal wind data from other global models or observations in the stratosphere. This will allow us to investigate what kind of gravity waves can propagate to where, since stratospheric winds have filtering effects on gravity waves with the same phase velocity as the wind speed. Although a simplified damping process for the gravity waves was added in the current model, the ultimate result of dissipation is that waves will break into turbulence. Wave breaking is the basis of material and energy transport in the mesosphere, e.g. meridional pole to pole circulation. It has been shown that a weaker pole to pole circulation is found due to the changing climate, which results in a warmer summer mesopause. To model the breaking of waves, non-linearity must be involved here which again requires high computational costs and the knowledge in the atmospheric dynamics.

Nevertheless, the outputs of the current forward model can be used in the evaluation of retrieval algorithm for processing measurements from MATS, especially in the tomographic reconstruction processes. The simulated images can also be used as an input signal to evaluate the optical design of the instruments on board, as well as other applications in the MATS project.

Bibliography

Brasseur, G. and Solomon, S. (2005). *Aeronomy of the Middle Atmosphere*, volume 53.

Campbell, I. and Gray, C. (1973). Rate constants for O(3P) recombination and association with N(4S). *Chemical Physics Letters*, 18(4):607–609.

DeMore, W. B., Sander, S. P., Golden, D. M., Hampson, R. F., Kurylo, M. J., Howard, C. J., Ravishankara, A. R., Kolb, C. E., and Molina, M. J. (1997). Chemical kinetics and photochemical data for use in stratospheric modeling. *JPL Publication*, 97-4(12):278.

Dörnbrack, A. and Nappo, C. J. (1997). A note on the application of linear wave theory at a critical level. *Boundary-Layer Meteorology*, 82(3):399–416.

Farman, J. C., Gardiner, B. G., and Shanklin, J. D. (1985). Large losses of total ozone in Antarctica reveal seasonal ClOx/NOx interaction. *Nature*, 315(6016):207–210.

Frederick, J. (1979). Influence of gravity wave activity on lower thermospheric photochemistry and composition. *Planetary and Space Science*, 27(12):1469–1477.

Garcia, R. R. and Solomon, S. (1983). A numerical model of the zonally averaged dynamical and chemical structure of the middle atmosphere. *Journal of Geophysical Research: Oceans*, 88(C2):1379–1400.

Garcia, R. R. and Solomon, S. (1994). A new numerical model of the middle atmosphere: 2. Ozone and related species. *Journal of Geophysical Research*, 99(D6):12937.

Hedin, A. E. (1991). Extension of the MSIS Thermosphere Model into the Middle and Lower Atmosphere. *Journal of Geophysical Research*, 96(A2):1159–1172.

Hines, C. O. (1960). Internal atmospheric gravity waves at ionspheric heights. *Can. J. Phys.*, 38:1441–1481.

Jonnes, A. V. (1974). *Aurora*. D.Reidel Publishing Company.

Liu, A. Z. and Swenson, G. R. (2003). A modeling study of O 2 and OH airglow perturbations induced by atmospheric gravity waves. *Journal of Geophysical Research*, 108(D4):4151.

Martin, L., Cohen, R. B., and Schatz, J. (1976). Quenching of laser induced fluorescence of O2 (b1Σg+) by O2 and N2. *Chemical Physics Letters*, 41(2):394–396.

McDade, I., Murtagh, D., Greer, R., Dickinson, P., Witt, G., Stegman, J., Llewellyn, E., Thomas, L., and Jenkins, D. (1986). ETON 2: Quenching parameters for the proposed precursors of O2(b1Σg+) and O(1S) in the terrestrial nightglow. *Planetary and Space Science*, 34(9):789–800.

Melo, S. M. L., McDade, I. C., and Takahashi, H. (2001). Atomic oxygen density profiles from ground-based nightglow measurements at 23°S. *Journal of Geophysical Research: Atmospheres*, 106(D14):15377–15384.

Mlynczak, G. and Olander, S. (1995). On the utility of the molecular oxygen dayglow emissions as proxies for middle atmospheric ozone. *Geophysical Research Letters*, 22:1377–1380.

Mlynczak, M. G., Solomon, S., and Zaras, D. S. (1993). An updated model for O2(a1Δg) concentrations in the mesosphere and lower thermosphere and implications for remote sensing of ozone at 1.27 μm. *Journal of Geophysical Research: Atmospheres*, 98(D10):18639–18648.

Murtagh, D., Frisk, U., Merino, F., Ridal, M., Jonsson, A., Stegman, J., Witt, G., Eriksson, P., Jiménez, C., Megie, G., de la Noë, J., Ricaud, P., Baron, P., Pardo, J. R., Hauchcorne, A., Llewellyn, E. J., Degenstein, D. A., Gattinger, R. L., Lloyd, N. D., Evans, W. F. J., McDade, I. C., Haley, C. S., Sioris, C., von Savigny, C., Solheim, B. H., McConnell, J. C., Strong, K., Richardson, E. H., Leppelmeier, G. W., Kyrölä, E., Auvinen, H., and Oikarinen, L. (2002). An overview of the Odin atmospheric mission. *Canadian Journal of Physics*, 80(4):309–319.

Murtagh, D. P. (1995). The state of O2 in the mesopause region. In *American Geophysical Union*, pages 243–249. American Geophysical Union.

Murtagh, D. P., Witt, G., Stegman, J., McDade, I. C., Llewellyn, E. J., Harris, F., and Greer, R. G. H. (1990). An assessment of proposed O(1S) and O2 (b 1Σg+)nightglow excitation parameters. *Planetary and Space Science*, 38(1):43–53.

Nastrom, G. D., Balsley, B. B., and Carter, D. A. (1982). Mean meridional winds in the mid- and high-latitude summer mesosphere. *Geophysical Research Letters*, 9(2):139–142.

Reed, E. I. and Chandra, S. (1975). The global characteristics of atmospheric emissions in the lower thermosphere and their aeronomic implications. *Journal of Geophysical Research*, 80(22):3053–3062.

Roble, R. G. and Dickinson, R. E. (1989). How will changes in carbon dioxide and methane modify the mean structure of the mesosphere and thermosphere? *Geophysical Research Letters*, 16(12):1441–1444.

Rothman, L. S., Jacquemart, D., Barbe, A., Benner, D. C., Birk, M., Brown, L. R., Carleer, M. R., Jr., C. C., Chance, K., Coudert, L. H., Dana, V., Devi, V. M., Flaud, J.-M., Gamache, R. R., Goldman, A., Hartmann, J.-M., Jucks, K. W.,

Maki, A. G., Mandin, J.-Y., Massie, S. T., Orphal, J., Perrin, A., Rinsland, C. P., Smith, M. A. H., Tennyson, J., Tolchenov, R. N., Toth, R. A., Auwera, J. V., Varanasi, P., and Wagner, G. (2009). The HITRAN 2008 molecular spectroscopic database. *Journal of Quantitative Spectroscopy and Radiative Transfer*, 110(9-10):533–572.

Sheese, P. E., Llewellyn, E. J., Gattinger, R. L., Bourassa, A. E., Degenstein, D. A., Lloyd, N. D., and McDade, I. C. (2010). Temperatures in the upper mesosphere and lower thermosphere from OSIRIS observations of O2 A-band emission spectra. *Canadian Journal of Physics*, 88(12):919–925.

Shepherd, G. G., Thuillier, G., Cho, Y.-M., Duboin, M.-L., Evans, W. F. J., Gault, W. A., Hersom, C., Kendall, D. J. W., Lathuillère, C., Lowe, R. P., McDade, I. C., Rochon, Y. J., Shepherd, M. G., Solheim, B. H., Wang, D.-Y., and Ward, W. E. (2012). The Wind Imaging Interferometer (WINDII) on the Upper Atmosphere Research Satellite: A 20 year perspective. *Reviews of Geophysics*, 50(2).

Slanger, T. G. and Black, G. (1979). Interactions of O2 (b1Σg+) with O(3P) and O3. *The Journal of Chemical Physics*, 70(7):3434.

A

Source code listing

A.1 Main-dayandnight-v6.m

```
clear; close all;

%% set wave parameters
Period = 1;
omega = 2*pi/(3600 * Period);
l_z = -5; %vertical wavelength [km] (Negative sign)
k_z = 2*pi / l_z; %vertical wavenumber [km-1]
k_hor = DR(omega, k_z); %horizontal wavenumber [km-1]
l_hor = 2*pi / k_hor; %horizontal wavelength [km]
zenithangle = 110;
angle_xi = 90; %choose angle of horizontal direction
angle_xi = deg2rad(angle_xi);
k_x = k_hor * cos(angle_xi);
k_y = k_hor * sin(angle_xi);
angle_xi = rad2deg(angle_xi);
A = 1; %reduced amplitude [km*s2]

disp('========Generating waves========')
disp(['Period is ', num2str(Period),'hour(s)']);
disp(['Vertical wavelength is ', num2str(l_z),'km']);
disp(['Horizontal wavelength is ', num2str(l_hor),'km']);
disp(['Reduced amplitude is ', num2str(A),'km*s2']);
disp(['Horizontal angle is ', num2str(angle_xi)]);
disp(['Soalr angle is ', num2str(zenithangle)]);

tic
%% set model domain
x = linspace(-200,200,101); %km
y = linspace(-670,770,145); %km
z = 70:0.5:150;
% t = linspace(0,Period*3600,10);
t = 0;
```

```
load msisdata.mat
month = 7;
lat = 10;
T = interp1(zMsis,TMsis(:,month,lat), z');
M = interp1(zMsis,NMsis(:,month,lat), z');
O2 = 0.2 * M;
N2 = 0.8 * M;
const = A .* sqrt(NMsis(1,month,lat)); %for wave amplitude

%% Parameters for [O] profile
OMax = 3e11; %oxygen peak concentration [molecule/cm3]
S = 0.8; %scale factor
H = 5.38; %scale height [km]
zmax = 98; % peak concentration height [km]
O = OxyShape(z, OMax, S, H, zmax)'; %[molecule/cm3]
clear OMax S H zmax latMsis monthMsis NMsis TMsis zMsis
clear prompt k_hor Period l_hor l_z lat month

%% Calculate Ozone for day
if abs(zenithangle) <= 100.6
   O(z<86) = O(z==86);
   O3 = mkozone(O, O2, N2, T, z, zenithangle);
   [Jhart,Jsrc,Jlya,JO3,~] = Jfactors(O, O2, O3, N2, ...
        zenithangle,x,y,z,t);
   gA = gfactor(O2, T, zenithangle, x, y, z, t);
end

%% Vectorise
[~, ~, Temp_Mean, ~] = ndgrid(x,y,T,t);
[~, ~, O_Mean, ~] = ndgrid(x,y,O,t);
[~, ~, M_Mean, ~] = ndgrid(x,y,M,t);
O2_Mean = 0.2 * M_Mean;
N2_Mean = 0.8 * M_Mean;
[hor_x, hor_y, alt, tim] = ndgrid(x,y,z,t);

%% Gravity wave model
Temp_Pertur_noDamp = TempPertur_noDamp(Temp_Mean, tim, ...
    hor_x, hor_y, alt, omega, k_x, k_y, k_z, const, M_Mean);
    %Temperature without damping

[Temp_Pertur, M_s, z_saturate] = TempPertur(Temp_Mean, ...
    tim, hor_x, hor_y, alt, omega, k_x, k_y, k_z, const,...
    M_Mean);
Aw = const ./ sqrt(M_s); % wave amplitude
O_Pertur = MinorPertur(O_Mean, tim, hor_x, hor_y, alt, ...
    omega, k_x, k_y, k_z, Aw);
```

```
O_Pertur_noDamp = MinorPertur(O_Mean, tim, hor_x, hor_y, ...
    alt, omega, k_x, k_y, k_z, const./sqrt(M_Mean));
M_Pertur = DensPertur(M_Mean, tim, hor_x, hor_y, alt, ...
    omega, k_x, k_y, k_z, Aw);
M_Pertur_noDamp = DensPertur(M_Mean, tim, hor_x, hor_y, ...
    alt, omega, k_x, k_y, k_z, const./sqrt(M_Mean));
O2_Pertur = DensPertur(O2_Mean, tim, hor_x, hor_y, alt, ...
    omega, k_x, k_y, k_z, Aw);
N2_Pertur = DensPertur(N2_Mean, tim, hor_x, hor_y, alt, ...
    omega, k_x, k_y, k_z, Aw);
[vel_x, vel_y] = VelocityHor(tim, hor_x, hor_y, alt, ...
    omega, k_x, k_y, k_z, Aw); % m/s
vel_z = VelocityVer(tim, hor_x, hor_y, alt, omega, k_x, ...
    k_y, k_z, Aw); % m/s
clear k_x k_y k_z omega A const tim hor_x hor_y alt const
clear O_Mean O2_Mean N2_Mean

vel_sqr = vel_x.^2 + vel_y.^2 + vel_z.^2; % v^2 [m2/s2]
Ek_Pertur = 0.5 * (M_Pertur*1e6) .* vel_sqr;
Ek_Mean = mean(mean(mean(Ek_Pertur,1),2),4);

%% Photochemistry model
if abs(zenithangle) <= 100.6
disp('=====Calculating dayglow volume emission rate=======')
ka = 6e-34 * exp(300./Temp_Pertur).^2.3;
kb = 8e-12 * exp(-2060./Temp_Pertur);
O3_Pertur = ka .* M_Pertur .* O2_Pertur .* O_Pertur ./ ...
    (JO3 + kb.*O_Pertur);

Vat_Pertur = dayglow(O_Pertur, O2_Pertur, O3_Pertur, ...
    N2_Pertur, Temp_Pertur, Jhart, Jsrc, Jlya, gA);
[Vat, Vat_from_O3, Vat_from_O2, Vat_from_barth, ...
    Vat_from_gA] = dayglow(O, O2, O3, N2, T, reshape(...
    Jhart(1,1,:,1),[],1), reshape(Jsrc(1,1,:,1),[],1),...
    reshape(Jlya(1,1,:,1),[],1), reshape(gA(1,1,:,1),[],1));
[~, ~, Vat_Mean, ~] = ndgrid(x,y,Vat,t);
clear ka kb gA Jhart Jlya Jsrc JO3 JO2

else
disp('===Calculating nightglow volume emission rate===')
Vat_Pertur = nightglow(O_Pertur, O2_Pertur, N2_Pertur, ...
    Temp_Pertur);
Vat = nightglow(O, O2, N2, T);
[~, ~, Vat_Mean, ~] = ndgrid(x,y,Vat,t);

end
```

```
save Vat.mat Vat_Pertur

%% HITRAN model
[Vat_ch1,Vat_ch2,ratio_ch] = AbandHitran(Vat_Pertur, ...
    Temp_Pertur);
[V_Mean_ch1,V_Mean_ch2] = AbandHitran(Vat_Mean, Temp_Mean);
ratio_Vat = Vat_ch1./Vat_ch2;

%% Limb radiance
alt_sat = 600; %altitude of the satellite orbit[km]
Int_pic_ch1 = satview(Vat_ch1(:,:,z<=110,1), x, y, ...
    z(z<=110), alt_sat);
Int_pic_ch2 = satview(Vat_ch2(:,:,z<=110,1), x, y, ...
    z(z<=110), alt_sat);
Int_pic_Mean_ch1 = satview(V_Mean_ch1(:,:,z<=110,1), x, y,...
    z(z<=110), alt_sat);
Int_pic_Mean_ch2 = satview(V_Mean_ch2(:,:,z<=110,1), x, y,...
    z(z<=110), alt_sat);
save satPic.mat Int_pic_ch1 Int_pic_ch2
```

A.2 DR.m

```
%% Dispersion relation
function k_y = DR(omega, k_z)

g = 9.8e-3; %gravitational acceleration [km/s2]
C = 340.29e-3; %speed of sound [km/s]
gamma = 1.4; %ratio of specific heats (c_p/c_v)

C1 = omega^4 * ones(size(k_z));
C2 = omega^2*C^2 * k_z.^2;
C3 = gamma^2*g^2*omega^2/4/C^2 * ones(size(k_z));
C4 = (1-gamma)*g^2 + omega^2*C^2;
k_y = sqrt((C1 - C2 - C3) ./ C4);
end
```

A.3 OxyShape.m

```
%% Atomic Oxygen profile parameterisation
function M_O = OxyShape(z, M_Omax, S, H, zmax)
zm = zmax * ones(size(z)); % peak  height [km]
```

```
M_O = M_Omax * exp(0.5 * (1 - (z-zm)./(S*H)...
    - exp((zm-z)./(S*H))));
end
```

A.4 mkozone.m

```
function O3_v = mkozone(O_v, O2_v, N2_v, T_v, z, zenitangle)

ka = 6e-34 * exp(300./T_v).^2.3;
kb = 8e-12 * exp(-2060./T_v);
M_v = O2_v + N2_v;

load sigma.mat
pathl = pathleng(z, zenitangle) * 1e5;  %[km -> cm]

%iter 1
tau = (O_v*sO' + O2_v*sO2' + N2_v*sN2')' * pathl';
JO3 = sum(irrad.*sO3 * ones(1,length(z)) .* exp(-tau))';
O3_v_a = ka .* M_v .* O2_v .* O_v ./ (JO3 + kb.*O_v);
%iter 2
tau = (O_v*sO' + O2_v*sO2'+ O3_v_a*sO3' + N2_v*sN2')'*pathl';
JO3 = sum(irrad.*sO3 * ones(1,length(z)) .* exp(-tau))';
O3_v_b = ka .* M_v .* O2_v .* O_v ./ (JO3 + kb.*O_v);
%iter 3
tau = (O_v*sO' + O2_v*sO2'+ O3_v_b*sO3' + N2_v*sN2')'*pathl';
JO3 = sum(irrad.*sO3 * ones(1,length(z)) .* exp(-tau))';
O3_v = ka .* M_v .* O2_v .* O_v ./ (JO3 + kb.*O_v);
```

A.5 TempPertur.m

```
%% Perturbed temperature in [K] and saturated altitudes
%temp: temperature [K]
%t: time [s]
%x,y: horizontal distance [km]
%z: altitude [km]
%omega: wave frequency [s-1]
%k_y, k_z: horizontal and vertical wavenumber [km-1]
%A: reduced amplitude [km*s2]
%M: density field [cm-3]
%M_s: density field for wave amplitude calculation

function [Tp, M_s, z_saturated] = TempPertur(T, t, x, y, ...
```

```
    z, omega, k_x, k_y, k_z, const, M)
% ==== constants ====
g = 9.8e-3; %gravitational acceleration [km/s2]
gamma = 1.4; %ratio of specific heats (c_p/c_v)
C = 340.29e-3; %speed of sound [km/s]
% ====================
theta = omega * t - k_x * x - k_y * y - k_z * z;
k_hor = sqrt(k_x^2 + k_y^2);
E2 = const ./ sqrt(M);
C1 = omega^2 * k_z;
C2 = g * (gamma * omega^2 / C^2 - k_hor^2);

T_dash = T .* E2 .* (gamma-1) .* (C1 .* cos(theta) - ...
    C2 * sin(theta));
T_dash(M == 0) = 0; % because of [k./sqrt(density)]
Tp = T + T_dash;

dT_dz = diff(Tp,1,3)./diff(z,1,3);
dT_dz(:,:,end+1,:) = dT_dz(:,:,end,:);
ELR = -dT_dz;
z_saturated = zeros(size(x,1),size(y,2),1,size(t,4));
for n_x = 1:size(x,1)
    for n_y = 1:size(y,2)
        for n_t = 1:size(t,4)
            z_s = find(ELR(n_x,n_y,:,n_t)>=10,1);
            if isempty(z_s) == 1
                z_s = size(z,3);
            end
            z_saturated(n_x,n_y,1,n_t) = z_s;
            M(n_x,n_y,z_s:end,n_t) = M(n_x,n_y,z_s,n_t);
        end
    end
end
M_s = M;
E2 = const ./ sqrt(M_s);
T_dash = T .* E2 .* (gamma-1) .* (C1 .* cos(theta) - ...
    C2 * sin(theta));
T_dash(M == 0) = 0;
Tp = T + T_dash;

end
```

A.6 DensPertur.m

```
%% Density perturbation
%density: density field [molecule/cm3]
%t: time [s]
%x,y: hosrizontal distance [km]
%z: altitude [km]
%temp: temperature field [K]
%omega: wave frequency [s-1]
%k_y, k_z: horizontal and vertical wavenumber [km-1]
%A: reduced amplitude [km*s2]
%Aw: wave amplitude

function Mp = DensPertur(M, t, x, y, z, omega, k_x, k_y,...
    k_z, Aw)

% ==== constants ====
g = 9.8e-3; %gravitational acceleration [km/s2]
gamma = 1.4; %ratio of specific heats (c_p/c_v)
C = 340.29e-3; %speed of sound [km/s]
H = 5.38 * ones(size(z)); %Scale height [km]
% ====================
theta = omega * t - k_x * x - k_y * y - k_z * z;
k_hor = sqrt(k_x^2 + k_y^2);
C1 = omega^2 * k_z;
C2 = (1 - gamma/2) .* k_hor^2 .* g;
C3 = omega^2 - k_hor^2 * C^2;

M_dash = M .* Aw .* (C1 * cos(theta) + (C2 + C3 ./ (2*H)) .*...
    sin(theta));
M_dash(M == 0) = 0;
Mp = M + M_dash;

end
```

A.7 MinorPertur.m

```
%% Minor gas density perturbation
%density: bulk density [molecule/cm3]
%t: time [s]
%x,y: hosrizontal distance [km]
%z: altitude [km]
%temp: vertical (or horizontal) temperature profile [K]
%omega: wave frequency [s-1]
%k_y, k_z: horizontal and vertical wavenumber [km-1]
```

```
%A: reduced amplitude [km*s2]
%Aw: wave amplitude

function nXp = MinorPertur(nX, t, x, y, z, omega, k_x, ...
    k_y, k_z, Aw)
% ==== constants ====
g = 9.8e-3; %gravitational acceleration [km/s2]
gamma = 1.4; %ratio of specific heats (c_p/c_v)
C = 340.29e-3; %speed of sound [km/s]
H = 5.38 * ones(size(z)); %Scale hight [km]
% ====================
theta = omega * t - k_x * x - k_y * y - k_z * z;
k_hor = sqrt(k_x^2 + k_y^2);

ddensity_dz = diff(nX,1,3)./diff(z,1,3);
ddensity_dz(:,:,end+1,:) = ddensity_dz(:,:,end,:);
E1 = ddensity_dz./ nX;
C1 = omega^2 * k_z;
C2 = (1 - gamma/2) .* k_hor^2 .* g;
C3 = omega^2 - k_hor^2 * C.^2;

nX_dash = nX .* Aw .* (C1 * cos(theta) + (C2 - C3 * (E1...
    + 1./(2*H))).*sin(theta));
nX_dash(nX == 0) = 0;
nXp = nX + nX_dash;

end
```

A.8 nightglow.m

```
function Vat = nightglow(O, O2, N2, T)
M = O + O2 + N2;
k1 = 4.7e-33 * (300./T).^2;
k2_O2 = 4e-17;% *1e-6; %[cm3s-1]
k2_N2 = 2.2e-15;% *1e-6; %[cm3s-1]
k2_O = 8e-14;% *1e-6; %[cm3s-1]
A1 =  0.079; %[s-1] HITRAN 1987
A2 = 0.083 * ones(size(M)); %[s-1] O2(1sig)
%=======Barth type reaction==================
O2star = k1 .* O .* O .* M; %O + O + M => Ostar + M
C_O = 19; % =33 when k2_O=0 (interpolated [O] with MSIS-83)
C_O2 = 6.6; %=7.5 when k2_O=0
Q = A2 + k2_O2 * O2 + k2_N2 * N2 + k2_O * O;
O21sig_barth =  O2star .* O2 ./ (Q .* (C_O * O + C_O2 * O2));
```

```
%=========================================================
Vat = A1 * O21sig_barth;

end
```

A.9 dayglow.m

```
function [Vat, Vat_from_O3, Vat_from_O2, Vat_from_barth, ...
    Vat_from_gA]= dayglow(O, O2, O3, N2, T, Jhart, Jsrc, ...
    Jlya, gA)

M = O + O2 + N2;
k1 = 4.7e-33 * (300./T).^2;
k2_O2 = 4e-17; %[cm3s-1]
k2_N2 = 2.2e-15; %[cm3s-1]
k2_O = 8e-14;% %[cm3s-1]
kc = 1.8e-11 * exp(110./T);
kd = 3.2e-11 * exp(70./T);
A1 =  0.079; %[s-1]
A2 = 0.083 * ones(size(M)); %[s-1]
A4 = 6.81e-3 * ones(size(M)); %O(1D) lifetime [s-1]

prodO1D_O3 = 0.9 * Jhart .* O3;
prodO1D_O2 = (Jsrc + Jlya) .* O2;
prodO1D = prodO1D_O3 + prodO1D_O2;
lossO1D = kc .* N2 + kd .* O2 + A4;
O1D = prodO1D./lossO1D; %[molecule/cm3]

% gA = gfactor(T,z,zenitangle,O2);
prodO21sig_O1D = 0.77*kd.*O2.*O1D;
prodO21sig_gA = gA .* O2;
lossO21sig = k2_N2 * N2 + k2_O2 * O2 + k2_O * O + A2;
O21sig_O1D = prodO21sig_O1D ./ lossO21sig; %[molecule/cm3]
O21sig_gA = prodO21sig_gA ./ lossO21sig;
%=======Barth type reaction=================
O2star = k1 .* O .* O .* M; %O + O + M => Ostar + M
C_O = 19; % =33 when k2_O=0  (interpolated [O] with MSIS-83)
C_O2 = 6.6; %=7.5 when k2_O=0
Q = A2 + k2_O2 * O2 + k2_N2 * N2 + k2_O * O;
O21sig_barth =  O2star .* O2 ./ (Q .* (C_O * O + C_O2 * O2));
%=========================================================

O21sig = O21sig_O1D + O21sig_gA + O21sig_barth;
Vat = A1 * O21sig;
```

```
Vat_from_O3 = A1 * O21sig_O1D .* prodO1D_O3 ./ (prodO1D);
Vat_from_O2 = A1 * O21sig_O1D .* prodO1D_O2 ./ (prodO1D);
Vat_from_barth = A1 * O21sig_barth;
Vat_from_gA = A1 * O21sig_gA;


end
```

A.10 pathleng.m

```
function [pathlength, columnpathl]= pathleng(heights, Xi)

%computes the pathlengths through atmospheric layers for rays
%incident on the layer given by the row index passing through
%the layers
%given by the column index for a solar zenith angle of xi.
%It also considers geometrical shading by the earth
%when zenitangles>90.

[m,n]=size(heights);
if n<m
        heights=heights';
end

length_heights = length(heights);
deltaz=heights(2:length_heights)-heights(1:length_heights-1);
deltaz=[deltaz deltaz(length(deltaz))];
heights=[heights max(heights)+deltaz(length(deltaz))];

nheights = length(heights);
Re=6370; % km Earth radius
d2r=pi/180;

if Xi==90
        Zt=heights;
else
        Zt=(Re+heights)*sin(Xi*d2r)-Re;
end

pathl=zeros(nheights);

for j=1:nheights
        h=heights(j:nheights);
```

```
        Ztj=Zt(j);
        pathl(j,j:nheights) = sqrt(h.*h+2*Re*(h-Ztj)-Ztj*Ztj);
end

pathl(:,1:nheights-1) = pathl(:,2:nheights) - ...
    pathl(:,1:nheights-1);
pathl=pathl(1:nheights-1,1:nheights-1);
pathl=triu(pathl);

pathlength = pathl;

heights=heights(1:(length(heights)-1));
nheights=nheights-1;

if (Xi>90)

    for j=1:nheights
        if Zt(j)>0
        I=find(heights<heights(j)&heights>Zt(j));

            if ((isempty(I)))
                I=max(1,j-1);

            else
                I=[max(I(1)-1,1) I];
                end

        h=heights(I)+deltaz(I);
        Ztj=Zt(j);
        pathl(j,I) = sqrt(h.*h+2*Re*(h-Ztj)-Ztj*Ztj);

            if (isempty(find(I==1, 1)))
            pathl(j,I)=(pathl(j,I)-pathl(j,max(I-1,1)));
            else
            J=I(I~=1);
            pathl(j,J)=(pathl(j,J)-pathl(j,max(J-1,1)));
            end

        elseif Zt(j)<=0
        pathl(j,:) = zeros(size(pathl(j,:)));

        end
end

pathl1=fliplr(pathl);
nanregion=find(isnan(pathl)==1);
```

```
pathl2=(triu((pathl'),1))';
pathl2(nanregion')=zeros(size(nanregion'));

pathlength=pathl+pathl2;
columnpathl=[pathl1 pathl2];
end
```

A.11 Jfactors.m

```
function [Jhart,Jsrc,Jlya,J3,J2] = Jfactors(O_v, ...
    O2_v, O3_v, N2_v, zenitangle,x,y,z,t)

load sigma.mat
pathl = pathleng(z, zenitangle) * 1e5;  %[km -> cm]
tau = (O_v*sO' + O2_v*sO2' + O3_v*sO3' + N2_v*sN2')'*pathl';

JO3 = irrad.*sO3 * ones(1,length(z)) .* exp(-tau);
JO2 = irrad.*sO2 * ones(1,length(z)) .* exp(-tau);
JO3(tau==0) = 0;
JO2(tau==0) = 0;

hartrange = wave>210 & wave<310;
srcrange = wave>122 & wave<175;
lyarange = 28; % wavelength = 121.567 nm
Jhart = sum(JO3(hartrange,:));
Jsrc = sum(JO2(srcrange,:));
Jlya = JO2(lyarange,:);

J3 = sum(JO3);
J2 = sum(JO2);

[~,~,Jhart,~] = ndgrid(x,y,Jhart,t);
[~,~,Jsrc,~] = ndgrid(x,y,Jsrc,t);
[~,~,Jlya,~] = ndgrid(x,y,Jlya,t);
[~,~,J3,~] = ndgrid(x,y,J3,t);
[~,~,J2,~] = ndgrid(x,y,J2,t);

end
```

A.12 gfactor.m

```
function gA = gfactor(O2, T, zenitangle, x, y, z, t)

load alines.dat
freq=alines(:,1);
Sj=alines(:,2);
Al=alines(:,3);
Elow=alines(:,4);
K = 1.3807e-23; %Boltzmann constant [m2kgs-2K-1]
C = 299792458; %speed of light [m/s]
AMU = 1.66e-27; %atomic mass unit [kg]

AD = freq/C *sqrt(2*log(2)*K*298/32/AMU);
grid=12900:0.01:13170; %frequency interval
sigma=zeros(length(z),length(grid));

for zi=1:length(z);
        Sjlayer=Sj*298/T(zi).*exp(1.439*Elow*(T(zi)-298)/...
            298/T(zi));
        ADlayer=AD*sqrt(T(zi)/298);
    for freqi=1:length(freq)
                sigma(zi,:)=sigma(zi,:) + Sjlayer(freqi) *...
                    doppler(ADlayer(freqi),grid-freq(freqi));
    end
end
path = pathleng(z,zenitangle);
tau = ((O2*ones(1,size(sigma,2))).*sigma)'*path'*1e5;
gA = sum((2.742e13*sigma'.*exp(-tau))./size(freq,1);
gA(tau(1,:)==0) = 0;
[~,~,gA,~] = ndgrid(x,y,gA,t);

end
```

A.13 doppler.m

```
%%Doppler broadening
function fi = doppler(AD, niu_niu0)
fi = sqrt(log(2)/pi)/AD * exp(-log(2)*niu_niu0.^2/AD^2);
end
```

A.14 VelocityHor.m

```
%% Horizontal Velocity in [m/s]
%t: time [s]
%x,y: hosrizontal distance [km]
%z: altitude [km]
%temp: vertical (or horizontal) temperature profile [K]
%omega: wave frequency [s-1]
%k_x, k_y, k_z: horizontal and vertical wavenumber [km-1]
%A: reduced amplitude [km*s2]

function [v_x,v_y] = VelocityHor(t, x, y, z, omega, k_x,...
    k_y, k_z, Aw)
g = 9.8e-3; %gravitational acceleration [km/s2]
C = 340.29e-3; %speed of sound [km/s]
gamma = 1.4; %ratio of specific heats
theta = -omega*t - k_x*x - k_y*y - k_z*z;
k_hor = sqrt(k_x^2 + k_y^2);
C1 = omega * k_hor * C^2;
C2 = ((1-gamma/2) * g / C^2);
v = Aw .* C1 .* (k_z*cos(theta) + C2*sin(theta)); %km/s
v_x = v * (k_x/k_hor) *1e-3; %m/s
v_y = v * (k_y/k_hor) *1e-3; %m/s

end
```

A.15 VelocityVer.m

```
%% Vertical Velocity in [m/s]
%t: time [s]
%x,y: horizontal distance [km]
%z: altitude [km]
%temp: temperature profile [K]
%omega: wave frequency [s-1]
%k_x, k_y, k_z: horizontal and vertical wavenumber [km-1]
%A: reduced amplitude [km*s2]

function v_z = VelocityVer(t, x, y, z, omega, k_x, k_y,...
    k_z, Aw)
C = 340.29e-3; %speed of sound [km/s]
theta = -omega*t - k_x*x - k_y*y - k_z*z;
k_hor = sqrt(k_x^2 + k_y^2);
C1 = omega *(omega^2 - k_hor^2*C^2);
v_z = Aw .* C1 .* cos(theta); %km/s
v_z = v_z *1e-3; %m/s
```

```
end
```

A.16 satview.m

```
function [Int_pic] = satview(Vol_ch, x, y, z, t, alt_sat)

R = 6370; %km earth radius
alt_bottom = 70;
alt_top = 110;

Sat = [0, -sqrt((R + alt_sat)^2 - ...
    (R + (alt_bottom + alt_top)/2)^2), ...
    R + (alt_bottom + alt_top)/2]; %satellite location

Px = -130:10:130; %tangent area (xOz plane)
Py = 0;
Pz = (R+alt_bottom):0.5:(R+alt_top);
[PX, PY, PZ] = ndgrid(Px, Py, Pz);

k = linspace(0.74,1.3,300); %points interval along the ray
lx = zeros(length(k),length(Px)*length(Pz));
ly = zeros(length(k),length(Px)*length(Pz));
lz = zeros(length(k),length(Px)*length(Pz));
for inter = 1:length(k)
    for i = 1:(length(Px)*length(Pz)) %number of rays
        lx(inter,i) = Sat(1) + k(inter) * (PX(i)-Sat(1));
        ly(inter,i) = Sat(2) + k(inter) * (PY(i)-Sat(2));
        lz(inter,i) = Sat(3) + k(inter) * (PZ(i)-Sat(3));
    end
end
dlx = lx(2:end,:)-lx(1:end-1,:);
dly = ly(2:end,:)-ly(1:end-1,:);
dlz = lz(2:end,:)-lz(1:end-1,:);
dl = sqrt((dlx).^2 + (dly).^2 + (dlz).^2);
dl(end+1,:) = dl(end,:); %pathlength in km

%=== change (x,y,z) to (alpha,beta,rho)
alpha = atan(lx(:,:) ./ lz(:,:));
beta = atan(ly(:,:) ./ lz(:,:));
rho = sqrt(lx(:,:).^2 + ly(:,:).^2 + lz(:,:).^2);
%=== query points(xq,yq,zq) ===
xq = alpha .* (R + alt_bottom);
yq = beta .* (R + alt_bottom);
zq = rho - R * ones(size(rho));
```

```
for n_t = 1:length(t)
    Vq = interpn(x,y',z, Vol_ch(:,:,:,n_t), xq,yq,zq,...
        'nearest', 0);
    V_int = sum(Vq.*dl,1);
    Int_pic = (reshape(V_int, [length(Px),length(Pz)]))';
end
```

B

Coefficients and constants adopted in the model

B.1 Rate coefficients

Reaction in the text	Coefficient	Reference
3.5	$k_a = 6 \times 10^{-34} exp(300/T)^{2.3}$	DeMore et al. (1997)
3.6	$k_b = 8 \times 10^{-12} exp(-2060/T)$	DeMore et al. (1997)
3.11	$k_1 = 4.7 \times 10^{-33}(300/T)$	Campbell and Gray (1973)
3.15	$k_2^{O_2} = 4.0 \times 10^{-17}$	Martin et al. (1976)
3.15	$k_2^{N_2} = 2.2 \times 10^{-15}$	Martin et al. (1976)
3.15	$k_2^{O} = 8.0 \times 10^{-14}$	Slanger and Black (1979)
3.25	$k_4^{N_2} = 1.8 \times 10^{-11} exp(110/T)$	DeMore et al. (1997)
3.26 and 3.27	$k_4^{O_2} = 3.2 \times 10^{-11} exp(70/T)$	DeMore et al. (1997)
3.16	$A_1 = 0.079$	Jonnes (1974)
3.17	$A_2 = 0.083$	Jonnes (1974)
3.28	$A_4 = 0.0068$	Jonnes (1974)

B.2 Other constants

Symbol	Physical meaning	Value	Unit
g	gravitational acceleration	9.8	m/s^2
C	speed of sound	340.29	m/s
γ	ratio of specific heats (c_p/c_y)	1.4	-
H	scale height	5.38	km
c	speed of light	3×10^8	m/s
k_b	Boltzmann constant	1.38×10^{-23}	$m^2\ kg\ s^{-2}\ K^{-1}$
m_{O_2}	molecule mass of O_2	5.3×10^{-26}	kg
h	Plank's constant	6.6×10^{-34}	$m^2\ kg/s$